Sensitivity analysis of a Venturi shaped structure for cross-flow turbines

Citation for published version:
Gabl, R, Burchell, J, Hill, M & Ingram, D 2022, 'Sensitivity analysis of a Venturi shaped structure for cross-flow turbines', *Engineering Applications of Computational Fluid Mechanics*, vol. 16, no. 1, pp. 2243-2269.
https://doi.org/10.1080/19942060.2022.2137850

Digital Object Identifier (DOI):
10.1080/19942060.2022.2137850

Link:
Link to publication record in Edinburgh Research Explorer

Document Version:
Peer reviewed version

Published In:
Engineering Applications of Computational Fluid Mechanics

ARTICLE

Optimisation of a Venturi shaped structure around a vertical axis tidal turbine

Roman Gabl[a], Joseph Burchell[a], Mark Hill[b] and David M. Ingram[a]

[a]School of Engineering, Institute for Energy Systems, FloWave Ocean Energy Research Facility, The University of Edinburgh, Max Born Crescent, Edinburgh EH9 3BF, UK;
[b]DHV Turbines Ltd, 272 Bath Street, Glasgow, G2 4JR, UK

ARTICLE HISTORY
Compiled May 20, 2022

ABSTRACT
Tidal energy is one of the worlds most predicable renewable energy sources and therefore holds great potential to be a valuable building block for the decarbonisation of the electricity production. This paper focuses on a vertical axis tidal turbine utilising a Venturi shaped outside structure (shroud) to accelerate the flow speed at the turbine. This concept is known as Davidson Hill Venturi (DHV) turbine. By constructing the nozzle and diffusor using hydrofoils, initial demonstrations indicate increased system efficiency. However, due to the potential number of hydrofoil geometric and structural variations, only a general description of the location of the hydrofoils is provided in order to facilitate modelling while allowing for future geometric variations to be devised. The conducted investigations focus on the influence of the nozzle and diffusor sections as the main geometry variations, identifing the length component in the orthogonal direction as the dominant parameter. A combined variation indicates higher velocity values are connected with larger forces, which must be supported by the devices structure. Slight improvements from the provided reference geometry were found as variations of hydrofoil placement and spacing were simulated. Thus, the main conclusion is that the reference geometry needs only small adaptations, which will be investigated further in a 3D-simulation study, including turbine interaction and rotation.

KEYWORDS
Tidal turbine; vertical axis; optimisation; Davidson Hill Venturi (DHV); ANSYS-CFX; SpaceClaim; Python;

1. Introduction

The kinetic energy of tidal currents are a renewable energy source, which is highly predicable and can provide a key component for the future fully de-carbonised electrical energy production (Bahaj, 2013; Khojasteh et al., 2022). A wide range of turbine concepts are currently investigated (Roshanmanesh, Hayati, & Papaelias, 2020). For example, they can be classified by the orientation of their rotation axis in vertical and horizontal axis turbines (Behrouzi, Nakisa, Maimun, & Ahmed, 2016; Khan, Bhuyan, Iqbal, & Quaicoe, 2009) or also in floating and bottom mounted devices. A wide range of different blades are used including open centre horizontal axis turbines (Belloni, Willden, & Houlsby, 2017; Borg, Xiao, Allsop, Incecik, & Peyrard, 2020, 2021),

CONTACT R.G.: roman.gabl@ed.ac.uk, J.B.: j.burchell@ed.ac.uk, M.H.: mark@tidalenergy.com.au

twisted blades (Mosbahi, Elgasri, Lajnef, Mosbahi, & Driss, 2021) or deflector blades (Patel & Patel, 2022). Blades can be either fixed, provide a variable pitch (Gu, Lin, Xu, Liu, & Li, 2018; H. Liu, Li, Lin, Li, & Gu, 2020) and/or yaw angle (Modali, Vinod, & Banerjee, 2021; qi Wang, Xu, qing Zhu, & Wang, 2018) or even change the shape (Pisetta, Le Mestre, & Viola, 2022) to further improve the efficiency. Further classifications can be made using the generator, nacelle types, supporting structure and generators (Roshanmanesh et al., 2020).

In addition to the turbine structure itself, various methods are available to increase the flow speed at the turbine and therewith improve the overall performance of the turbine. For example, Z. Liu, Wang, Shi, and Qu (2019) investigates four additional hydrofoils placed as a guide-vane diffuser using ANSYS-Fluent. Hua-Ming, Xiao-Kun, Lin, Lu-Qiong, and Qiao-Rui (2020) used the software STAR-CCM+ to investigate different ducts in a current flow limited by close side banks. This investigation was conducted as a 3D simulation but without a turbine present. A three bladed vertical axis turbine was simulated by El-Sawy, Shehata, Elbatran, and Tawfiq (2022) under river conditions. An integration in a floating configuration is also possible (Hardisty, 2008). More commonly used for free stream turbines is a diffusor similar to the ones for wind turbines (Arumugam, Ramalingam, & Bhaganagar, 2021; Noorollahi, Ghanbari, & Tahani, 2020; Nunes, Brasil Junior, & Oliveira, 2020). Those structures can be optimised for on single flow direction or allow a bi-directional usage (Fleming & Willden, 2016), which enables a fixed installation. Such ducted geometries can be very simple structures but also include a variety of complex shapes and combined structures, as investigated by Huang et al. (2022). This paper investigates a Venturi shaped structure, which assembles multiple hydrofoils in order to accelerate the available flow through the vertical axis turbine (Kirke, 2011). A summary of shapes and the influence of diffusors and horizontal axis turbines can be found in Nunes et al. (2020). Walker and Thies (2021) indicates the percentage of failed tidal turbines, are higher hence the loads due to the increased velocity are higher. Nevertheless, they indicated that with improved materials and optimised concepts the potential of ducted turbines can be significant.

Ongoing research challenges can be found in the simulation of the turbine itself, which can be simplified by various approximations (Baratchi, Jeans, & Gerber, 2020). Ke, Wen-Quan, and Yan (2020) compares bares a horizontal axis turbine with a range of diffusors under a distributed inlet velocity as well as the interaction of multiple turbines in an array. Multiple vertical axis turbine arrays are investigated by Sun, Ji, Zhang, Li, and Wang (2021). Ahmed, Apsley, Afgan, Stallard, and Stansby (2017) studied the influence of the velocity distribution and compared it with field data and Badshah, Badshah, and Kadir (2018) used a Fluid-Structure-Analysis to quantify the influence of a realistic velocity distribution in relation to a homogeneous approach.

The overall design of tidal turbines is strongly reliant on numerical simulations (Nachtane, Tarfaoui, Goda, & Rouway, 2020). Additional, experimental investigations allow specific measurement data to be compared leading to improvements within the numerical models. A good example can be found in the paper by Badoe et al. (2022), who simulated up to three tidal turbines under a comparable complex flow conditions representing the unique FloWave Ocean Energy Research Facility (part of the University of Edinburgh). This facility provides a raisable floor for the dry installation of not only tidal turbine model and ensures a highly repeatable flow condition of up to 1.6 m/s rotatable by 360° due to the circular arrangement of the flow drives. W. Liu et al. (2022) validated their numerical model of a diffuser-augmented tidal turbine with a towing tank experiment. Feng et al. (2022) used a flume to compare the wake interaction between two ducted horizontal axis turbines. Obviously, the next step for the validation is the deployment of the optimised structure combined with a competitive measurement system to reduce the uncertainties in the validation.

The presented research work uses a similar approach to Maduka and Li (2021), who investigated a ducted vertical turbine using a reduced 2D-approach and simplified the turbine with an actuator disc approach in the numerical software OpenFOAM. In contrast to this, the current paper focuses on an application of a ducted vertical axis tidal turbine and introduces a basic description of the Venturi shaped shroud of the Davidson Hill Venturi (DHV) turbine. The supporting structure of the turbine device is in part assembled using hydrofoils arranged either side of the inlet, parallel to the axis of the turbine, improving the acceleration of the flow at the turbine. All numerical simulations are conducted with a commercial code ANSYS-CFX. The geometry generation is provided in the SpaceClaim specific IronPython as well as the open Python code (Gabl, Burchell, Hill, & Ingram, 2022). This ensures that the conducted variations can be reproduced and expanded with any solver. The methodology is described Section 2, which includes a reference geometry (Sec. 2.4) as well as the verification of the 2D-numerical simulation (Sec. 2.6). A key output of the paper is the variation of the main geometry parameters as well as the embedded hydrofoils (Sec. 3). Section 4 provides a discussion of the chosen methodological approach. The investigation is conducted with a reduced complexity of numerical simulations and allow the identification of the optimum shape, which will be further numerically tested in a fully 3D-setup to bring this concept closer to a commercial deployment producing fully predicable renewable energy from river, canal and tidal flows.

2. Materials and methods

2.1. Overview

A standard tidal turbine requires the blades, generator and support structure. One of the unique features of the Davidson Hill Venturi (DHV) turbine is the outer structure, which contains multiple hydrofoils forming a Venturi channel (DHV Turbines Ltd, 2022; Kirke, 2011).This concept was invented by Aaron Davidson and Craig Hill and is commercialised by DHV Turbines Ltd. The smallest cross sectional area occurs at the turbine position, which augmentates the incoming flow resulting in increased fluid velocities acting on the turbine. As part of the ongoing research work, a generalised geometry description is suggested, providing the current conducted parameter variation as well as future additional work. The conducted numerical simulations are limited to a 2D-approach and focuses on the guide structure only, neglecting interaction with the turbine. Section 2.2 introduces the solver and basic numerical settings. A local coordinate system is introduced in Section 2.3 for the geometry description, shown as the reference geometry in Section 2.4. The wide range of numerical results are analysed, with primary focus on the turbine cross section (Sec 2.5). Section 2.6 summarises the key aspects of the verification process, namely the size of the fluid domain and the mesh test. All these components are required for the variation of the geometry presented in Section 3 and a discussion of the methodology can be found in Section 4. The optimised geometry will be further numerically investigated and refined, with future experimental investigation and deployment required in order to validate the modelling data.

2.2. Solver and numerical settings

The presented numerical investigation uses the commercial Computational Fluid Dynamic (CFD) software ANSYS-CFX (version 2020 R2). This software was used for a wide range of numerical studies in specific aspects of tidal turbines. Sun et al. (2022) found that a four bladed vertical axis turbine brings significant advantages in the starting performance based on simulations with CFX. Sun, Ma, Wang, and Li (2019) focused on the fluctuation of the angular speed and also conducted specific validation experiments in the laboratory. Rehman et al. (2021) investigated the wake behind a single horizontal axis turbine utilising this software and Allmark et al. (2020) integrated it into the design and blade optimisation of a scaled turbine. In combination with other ANSYS products, further capabilities to couple physics and conducted Fluid-Structure-Interaction (FSI) simulations are attainable, as shown by Badshah, Badshah, and Jan (2020) and Ullah et al. (2019). While a key application area of the software is the investigation and optimisation of turbines (Mulu, Cervantes, Devals, Vu, & Guibault, 2015; Picone, Sinagra, Aricó, & Tucciarelli, 2021), a wide range of further applications can be found (Lee, Seong, & Kang, 2018; Richter et al., 2021). Recent validation experiments include the optimisation of an inlet-outlet structure (Bermúdez et al., 2017) and spillway (Andersson, Andreasson, & Lundström, 2013). The high degree of validation within the numerical solver allows this paper to focus fully on the verification as presented in Section 2.6.

All simulations use the assumption of a 2D-approach, which is realised by a single cell size in the vertical z-direction. The size of the fluid domain is chosen based on the verification process presented in the Section 2.6. A constant homogeneous velocity is set at the inlet face. Nominally the inlet speed is set to 1 m/s, however for completeness the effect of speed variation is assessed and can be found in Section 3.9. On the opposing side of the fluid domain, the outlet is set as a pressure outlet with a constant static pressure of 1 bar to ensure that cavitation is not an issue. All other sides of the fluid domain box are set to symmetry with the investigated structure allocated wall (no slip wall option with a roughness setting of smooth wall). The simulated fluid is standard water (density = 997.0 [kg m^{-3}]), while isothermal approach is used at a constant temperature of $10°C$. No buoyancy is considered.

The standard steady state solver computes the Reynolds-Averaged Navier-Stokes (RANS) equations, while the closure problem is solved based on the Shear Stress Transport (SST) turbulence model (F. Menter, 1993, 1994; F. R. Menter, Kuntz, & Langtry, 2003). This turbulence model blends a $k - \omega$ and $K - \epsilon$ turbulence model to combined the advantage of each specific model. The SST model is widely used for a broad range of solver (Cindori, Čajić, Džijan, Juretić, & Kozmar, 2022; He, Zhao, Wan, & Wang, 2022; Sarkar & Savory, 2021; Yi, Wang, Sun, Huang, & Zheng, 2017). Due to the fact that the geometry is varied in a significant way and introduces different flow regimes, the auto time scale function of the solver is used with a time scale factor of 1. For some exemplary cases a modification to 0.1 and 10 was investigated, which resulted in a slower convergence behaviour of the numerical solution. The solver runs in all cases using double precision to reduce the potential influence of rounding errors. Three additional monitor points of velocities in the cross section of the turbine are used to ensure that the solution is converged and can be stopped. Further verification studies can be found in Section 2.6.

2.3. *Local coordinate system*

A local coordinate system is defined so that the z-axis is coincident to that of the vertical axis turbine. The positive x-axis is orientated along the main flow direction resulting in a positive velocity. Thus the x-z-plane is the symmetry plane for the geometry and the y-axis aligns according to the right handed coordinate system. The origin for the 2D-dimensional simulations was placed on the bottom part of the axis.

2.4. *Reference geometry and parameters*

The overall geometry of the DHV turbine includes a large number of variables, with each having significant impact on the overall efficiency, production cost and maintenance of the turbine. In order to reduce the number of parameters within the design, the first step focuses on the outer Venturi structure and assumes that the turbine itself can be optimised in a following assessment. Similar assumptions are made for the support structure. The previously conducted experimental and numerical investigations ensured the principal validation of the turbine concept (Kirke, 2006, 2011) as well as a fair amount of parameter variations. A full investigation of all parameters and combinations would exceed the time frame of any research project. Hence, a limited amount of combinations are investigated starting from the later described reference geometry. Nevertheless, a key step is the full parametrisation of the geometry so that the later gained results can be easily documented, reproduced and expanded upon. The decision was made to provide this in the from of a Python code, which is available in Gabl et al. (2022). This also publishes a specific IronPython version, which is allows for the geometry definition in 3D CAD modelling software SpaceClaim. Therewith a full integration in the ANSYS WORKBENCH is possible and the fluid solver ANSYS-CFX was used for this project.

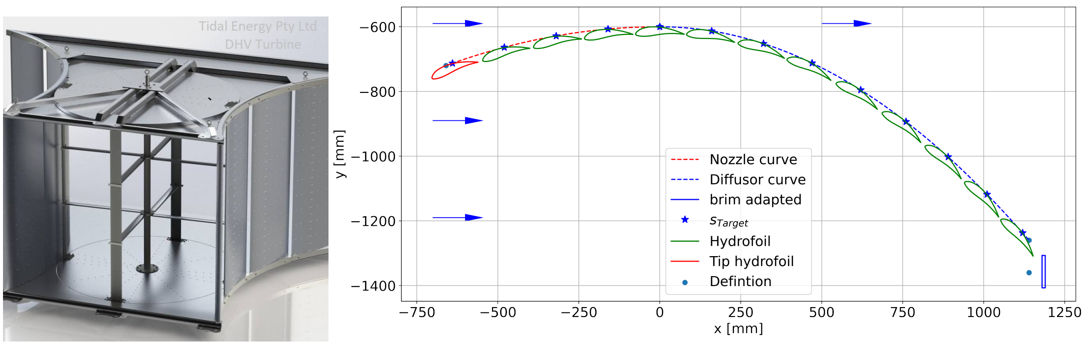

(a) Previous design

(b) Reference geometry

Figure 1. Overview of the previous design (a) provided by DHV Turbines Ltd and the half side of reference geometry (b) and the vertical axis turbine rotating in the origin of the coordinate system

For the following geometry investigation an initial reference geometry (Figure 1 (b)) was utilised, based on a previous DHV demonstrator project. These values are presented in combination with the specific geometry parameters as follows:

- One of the defining parameters of the housing geometry is the radius of the vertical axis turbine R_{Turb}. It is chosen to 0.6 m for the reference geometry and later used to standardise all length of the geometry.
- Both sides of the Ventri channel are symmetrical along the x-z-plane and split

at the y-z-plane (turbine location) in two parts: nozzle and diffusor. As shown in Figure 1 (b), this shape is defined by three points for the main curves. The centre one is defined by the turbine with R_{Turb} and the coordinates of the outer two points are defined by the R_{Front} and L_{Front} as well as R_{Back} and L_{Back}. In the case of the reference geometry, shown in Figure 1 (b), the combination of [R_{Front},L_{Front},R_{Back},L_{Back}] equal [1.2,1.1,2.1,1.9] $\cdot$ R_{Turb} was chosen. The radius describes the distance/length in the y-direction according to the local coordinate system.

- A bell curve is defined between these points, chosen based on the Alkhabbaz, Yang, Tongphong, and Lee (2022), which includes the work of Khamlaj and Rumpfkeil (2018b, 2018a). Eq. (1) presents the nozzle (with a negative x-value indicated by x_{neg}) and diffusor (x_{pos}) part aligned along the flow direction on the right side of the geometry (Fig. 1 (b)).

$$\begin{aligned} y_{neg} &= R_{Turb} - 1 - x_{neg}^2 \cdot (R_{Front} - R_{Turb})/L_{Front}^2 \\ y_{pos} &= R_{Turb} - 1 - x_{pos}^2 \cdot (R_{Back} - R_{Turb})/L_{Back}^2 \\ with\ &-1 \cdot L_{Front} \leq x_{neg} \leq 0\ and\ 0 \leq x_{pos} \leq L_{Back} \end{aligned} \tag{1}$$

- The hydrofoil profiles are then located to these curved forms. For the reference geometry a GOE 222 (MVA H.33) AIRFOIL (Airfoil Tools, 2022) with a chord length c_{Foil} of 150 mm was chosen. The local reference point for the hydrofoil is placed at the mid point of the chord length at the maximum height (Gabl et al., 2022). This ensures that the hydrofoil does not interfere with the cross sectional area of the turbine. Downstream of the central position on each side, the bell curves split into segments with a constant chord length of s_{Target} equal 160 mm. The implementation is shown in Gabl et al. (2022) and results in an integer number of hydrofoils for each side. As shown in Figure 1 (b), the individual reference point for the last hydrofoil is still inside of the definition point but the hydrofoil reaches outside of the curve. Limiting the design to one single size hydrofoil with constant chord spacing might swallow smaller geometry changes but seems to be more practical than variations of the hydrofoil sizes. Variable hydrofoil size would result in significant higher cost of the structure. Furthermore, each hydrofoil is rotated based on the differential of the curve to ensure that the tangential direction is similar to the bell shape. Additional variables, which allows for a constant changes to the angle of attack of all hydrofoils as well as a specific modification of the first hydrofoil (red foil in Fig. 1 (b)) in the flow direction, are included in the Python code. The additional angle of the orientation of the first hydrofoil in the flow direction is investigated in Section 16.
- In addition to the hydrofoils, a brim is included in the reference geometry. The height (y-direction) is 100 mm and the thickness is 10 mm. These values were primarily chosen to be small but still clearly have an influence in the mesh generation. A specific investigation of the size of the additional brim is presented in Section 3.3.

The last two noteworthy aspects of the geometry definition, namely the hydrofoils as well as the brim, are clear differences to the previous tested design of the DHV turbine. In some aspects a smaller hydrofoil has advantages compared to the larger profiles previously deployed. Smaller shapes can be extruded (ideal for a mass production) instead of welding single pre-cut parts. In the original configuration of the DHV turbine a brim structure was absent from the design. A wide range of investigations show the efficiency of such an additional blockage element for wind turbines (Alkhabbaz et al., 2022; Arumugam et al., 2021; Khamlaj & Rumpfkeil, 2018b, 2018a; Nunes et al., 2020). To test the influence in the case of a DHV turbine a small brim section is initially added on both sides at the end of the bell shape. Its upstream edge, closest to the symmetry plane, is similarly placed to the reference points of the hydrofoils but, with half the chord distance Δs_{Brim} equal to 80 mm. The variation of the geometry is discussed and the results are presented in Section 3.

2.5. Post-Processing

The post-processing of the numerical results focuses on the velocity distribution represented by the variable vel. The actual flow direction is not considered and further detailed analysis can be used for the evaluation of the full geometry (Gabl, Achleitner, Neuner, & Aufleger, 2014). Three different control sections are defined. One full cut through the fluid domain as a y-z-plane (coordinate system is described in Sec 2.3) with an x-value of -3 m for the inflow conditions and another at x=6 m for the outflow. The main control cross section is set in the centre of the turbine axis orientated in the y-z-direction but limited to R_{Turb}+10 mm to each side. This allows specific analyse the flow between the two structures at the location of the turbine. Values referencing this cross section are indicated with the index $_c$. The other two cross sections are used for the verification of the inflow and outflow and are not specifically reported in this paper. For the main analysis the following parameters are used:

- area-averaged velocity at the turbine cross section $\overline{vel_c}$ using the ANSYS CFD-Post function $areaAve(vel)$
- total forces in x-direction F_x based on the calculation $sum(Force\ X)$
- kinetic energy flux coefficient α_c based on the Eq. (2)
- extreme values (minimum and maximum) of vel_c

The first two values, namely $\overline{vel_c}$ and F_x, are the main parameters for the analysis presented in Section 3. The average of the full cross section was deliberately used for the velocity value, while the velocity distribution was evaluated with the help of the α_c-value. This coefficient, which is used to correct the standard Bernoulli's equation for the real kinetic energy $E_{kin,real}$, is typically larger than the homogeneous approach for the theoretical value $E_{kin,theo}$. Fully developed laminar flow in a pipe cross section results in a parabolic velocity distribution and a α-value of 2. Typical turbulent flows are in the range of 1.2 (Gabl et al., 2014; Gabl & Righetti, 2018; Ward-Smith, 1980). The α-value is calculated based on the following equation:

$$\alpha_c = \frac{E_{kin,real}}{E_{kin,theo}} = \frac{1}{A} \cdot \int_A \left(\frac{vel}{vel_m} \right)^3 dA \qquad (2)$$

This equation can be included in ANSYS CFD-Post using the CFX Expression Language, or CEL, as an expression with the location *Plane2* references the cross section at the turbine:

```
alphaC = areaInt(vel^3)@Plane2/((areaAve(vel)@Plane2)^3*area()@Plane2)
```

In addition to this global evaluation value, the minimum and maximum value of the cross section is analysed to find the range of the flow velocities at the turbine. Note that the α and extreme values are only shown if they are particular interesting for the analysis. Section 3 includes example analysis of velocity contour plots. Those plots always show the x-y-plane and the influence of the z-direction can be neglected due to the a 2D nature of the simulation. If not otherwise stated, the colour bar for the velocity plots are limited from 0 to 3.5 m/s, which allows ease of comparison between the various geometry investigations provided.

2.6. Verification

The verification process includes an investigation of the fluid domain size based on a first pass approximation of the computation mesh, which was subsequently modified in a second step. A compromise between the distance of the boundary conditions to the main investigated part as well as the overall computational cost of the simulations is targeted, while ensuring that the resulting outcomes are independent of the chosen mesh input variable. For all presented simulations, the reference geometry was investigated as introduced in Section 2.4. The derived variables and analyses are presented in Section 2.5.

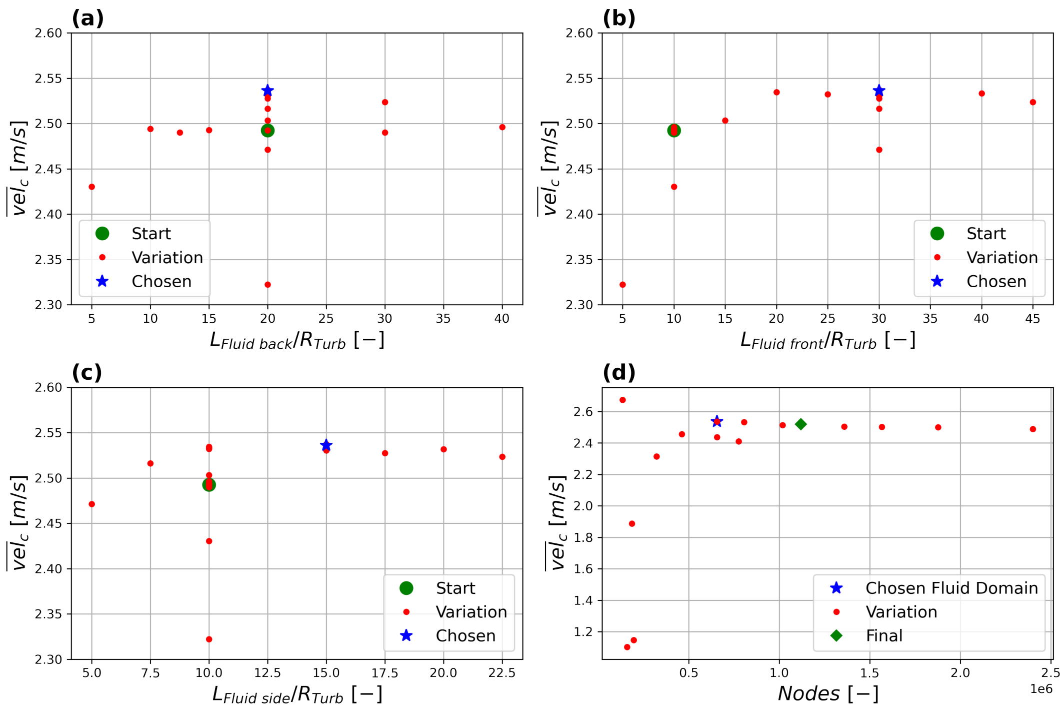

Figure 2. Summary of the verification process with a specific mark of the start as well as the final chosen value — (a-c) present the full set of fluid domain changes but as a result of to the individual investigated length — (d) comparison of the different investigated meshes.

An initial volume for the fluid domain was chosen based on a rectangular cuboid with three length (all referenced from the origin of the local coordinate system, Section 2.3) and a thickness. The near side length $L_{Fluid\ front}$ defines the dimension in the negative x-direction and was initial chosen to be equal $10 \cdot R_{Turb}$. While, both sides were extended out to $L_{Fluid\ side}$ of $10 \cdot R_{Turb}$ from the symmetry plane, resulting in a total width of $20 \cdot R_{Turb}$. The downstream part of the fluid domain was expanded with a length of $L_{Fluid\ back}$=$20 \cdot R_{Turb}$. This values is highlighted as a starting value in the graphs provided in Figure 2 (a-c). All three graphs show the same outputs but mapped against the alternative investigated lengths. To start with, the downstream section of the fluid domain was varied. Figure 2 (a) shows that the range of 10 to 40 $\cdot$ R_{Turb} results in very similar values for the chosen indicator $\overline{vel_c}$. The upstream section was chosen to be too short in the first assumption and hence expanded to 30 $\cdot$ R_{Turb}. Similarly, the side lengths were expanded to 15 $\cdot$ R_{Turb}. All dimensions were deliberately increased to accommodate the expansion of the bell shapes and any expected modifications of the geometry. The total thickness of the fluid domain was set to the depth of a single cell of 10 mm, thus resulting in a 2D-simulation. The thickness (fluid domain in the z-direction) was modified to 5 and 100 mm, which had no influence on the velocity distribution.

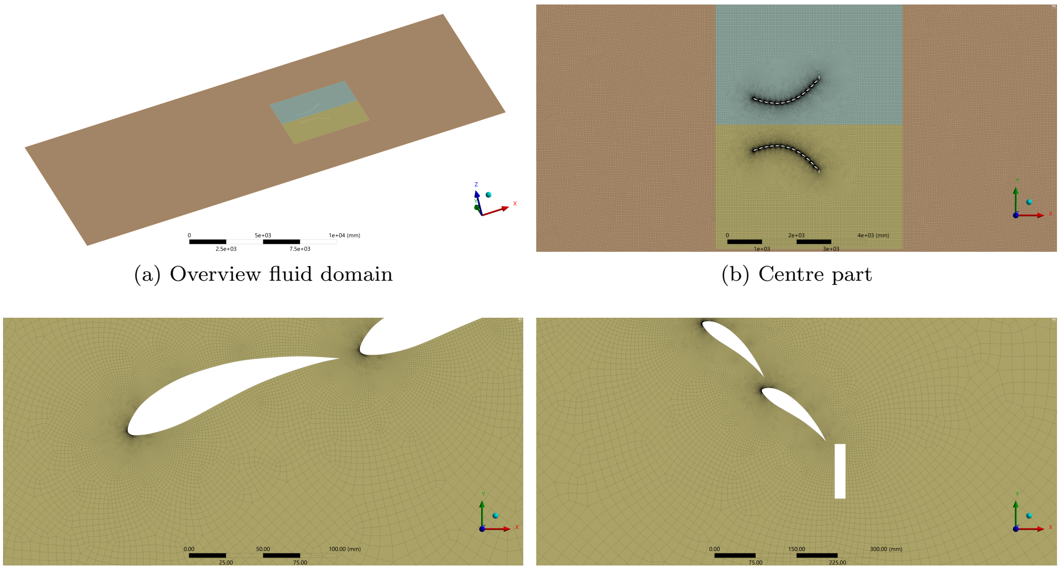

(a) Overview fluid domain

(b) Centre part

(c) Detail first hydrofoil

(d) Detail last hydrofoil and brim

Figure 3. Final meshing used for the 2D-investigation using the reference geometry.

Following the variation of the fluid domain, the meshing strategy and resolution was modified. Figure 2 (d) presents the overview of the conducted mesh test. All meshes were 2D-dimensional with one cell height in the z-direction. Due to the automated geometry generation and high degree of variability, only global mesh parameters were set, which influence the complete fluid domain. The final mesh deploys the following settings with the chosen values: Element size (50 mm), growth rate (1.05 [-]), max size (100 mm), defeature size (0.05 mm), curvature min size (0.05 mm) and curvature normal angle (0.5 deg). The MultiZone method was used to fill the fluid domain with hexagonal shaped cells and in total the mesh included over 1.1. million nodes. Due to the fact that this meshing method is limited to a single core, mesh generation took a comparably long time and the decision was made to split the complete fluid domain in three sub domains. As shown in Figure 3, each side of the geometry is cut out with a total length in x-direction of 9 $\cdot$ R_{Turb} (3 upstream and 6 $\cdot$ R_{Turb} downstream of the turbine axis) and individual width of 6 $\cdot$ R_{Turb}. This results in an interface boundary but allows to distribute the mesh generation to more processors.

As a final assessment the selected mesh was run within the fluid domain, which was expanded by the factor 1.5 in the x-y-plane. For this expanded case the area-average value of the velocities at the turbine were smaller by 0.01277 m/s representing 0.504% of to the original average value.

3. Results

3.1. Overview

The presented results can be grouped into four different categories: (a) the shape of the bell curve described by the definition points, (b) the angle of the first hydrofoil, (c) the shape and size of the hydrofoils and (d) the inflow velocity, which is presented in the Section 3.9.

An overview of the major variation grid for the nozzle and diffusor part is shown in Figure 4. The reference value, presented in Section 2.4, is marked. This figure also provides the tangential angle of the hydrofoil to the outside of the bell curve. In addition to the colour bar, two exemplary values are marked with 10 and 55° as a reference. The latter presented results also include further refinement, however, this is not included in this overview. Both parts are varied separately, while the other side is kept at the reference geometry. Section 3.2 presents the variation of the nozzle geometry and the investigation of the diffusor is combined with the extension of the brim in Section 3.3. For all those variations the radius of the vertical turbine R_{Turb} is kept constant at 600 mm. Section 3.4 provides the investigation of this parameter in two ways and compliments the geometry variation. The narrowing of the structures geometry resulted in an interesting result, which is further investigated in Section 3.5 by scaling both sides of the structure with a constant factor. In addition, the angle of the first hydrofoil in the flow direction is investigated in Section 3.6.

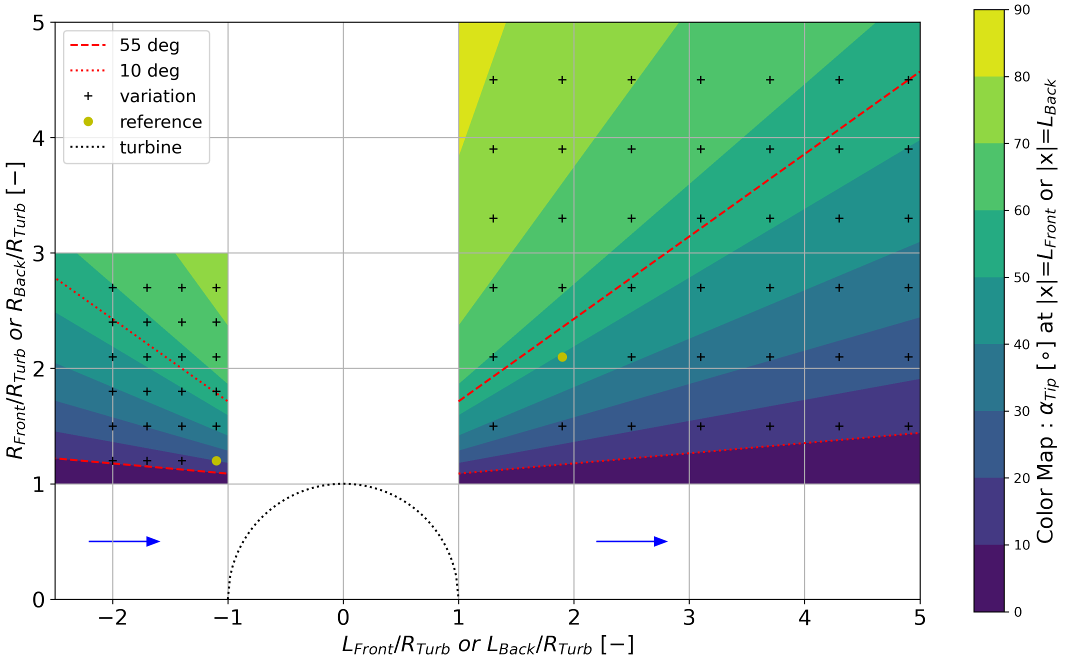

Figure 4. Overview of the main grid for the geometry variation normalised by the turbine radius R_{Turb} with a colour map of the angle α_{Tip} of the first (for the nozzle) or last hydrofoil using this definition point. A value of $\alpha_{Tip} = 0°$ indicates orientation along the x-axis and 90° along the y-axis. The reference value is described in Section 2.4.

The second main group of the variation is the investigation of the hydrofoils itself. Section 3.7 scales the length of the individual hydrofoil as well as the distance between the standard foil. Up to this point, all simulations are conducted with a hydrofoil profile based on the GOE 222 Airfoil (Airfoil Tools, 2022) and only within Section 3.8 is the hydrofoil geometry changed. Due to various factors, it was assumed that only one single type of hydrofoil is used at any time in the variation. A discussion of the used methodological approach is provided in Section 4.

3.2. Variation of the nozzle

The first variation of the geometry is to alter the the nozzle of the Venturi structure. For those cases, the downstream part is fixed with reference values, as described in Section 2.4. The results for this variation are provided in Figure 5, which presents the area-average velocity value $\overline{vel}_c$ of the turbine cross section in the upper row and the total forces F_x in the x-direction. Note that the latter is normalised by the reference value. Each graph shows the same numerical results but, the left column presents it in relation to the standardised value of the inlet radius R_{Front} and the length L_{Front} in the right column of Figure 5. A variation grid of 180 mm ($0.3 \cdot R_{Turb}$) was investigated for both variables defining the inlet bell. In addition, specific addition points were run to further investigate specific combinations and enrich specific parts with a high gradient.

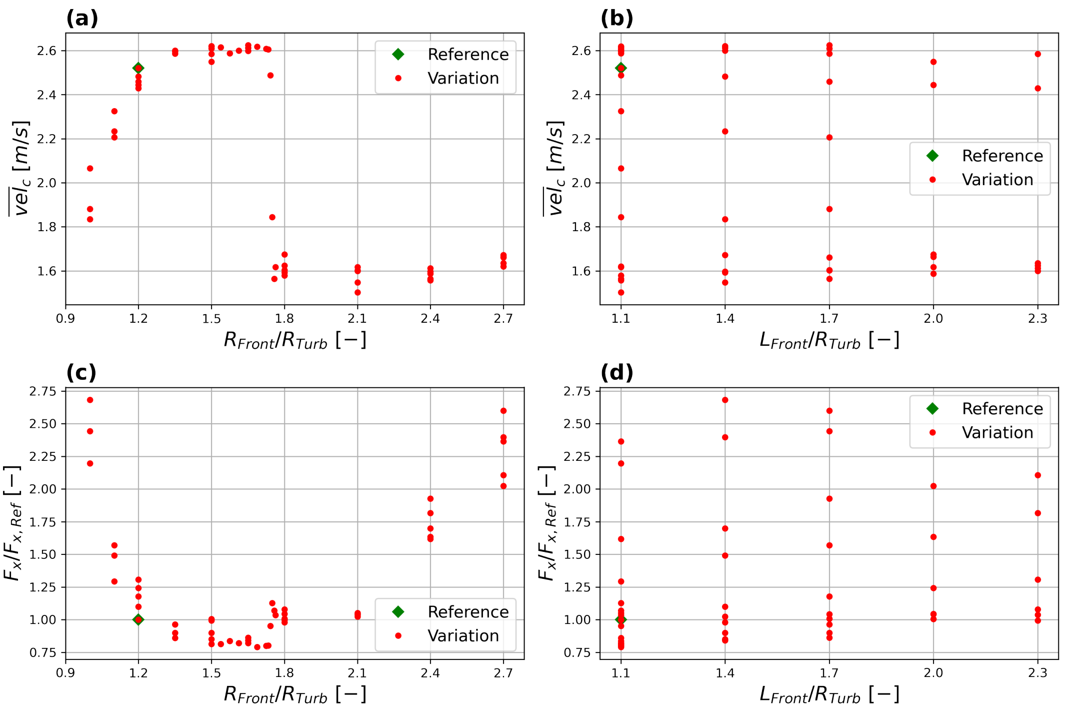

Figure 5. Variation of the nozzle with a fixed diffusor $[R_{Back}, L_{Back}] = [2.1, 1.9] \cdot R_{Turb}$ — area-averaged velocity at the turbine cross section $\overline{vel}_c$ depending on the opening radius R_{Front} (a) and sorted by the length L_{Front} (b) — Forces in x-direction F_x standardised by the reference value (c-d) — all length standardised by the turbine radius R_{Turb}.

By varying R_{Front} and length L_{Front} and comparing the outcomes, the dimension in the orthogonal direction to the main flow direction, namely R_{Front}, is shown to have a significant influence. Figure 5 (a) indicates that an increasing opening width R_{Front} results in an increasing area-averaged velocity at the turbine cross section $\overline{vel}_c$ up to a certain level, which is followed by a drop in the efficiency of the inlet structure. This specific section is refined down to a level of 5 mm steps for the R_{Front}. The jump occurs for a R_{Front} value in the range of $1.74583 \cdot R_{Turb}$ (between 1045 and 1050 mm). In reality, such close points would not be advisable as construction tolerances could potentially have a significant influence of the turbines operation. Therefore, a higher level can be achieved starting with $1.5 \cdot R_{Turb}$ in order that the aforementioned jump can be avoided.

The total force in the x-direction F_x acting on the structure increases for both smaller and larger values with a minimum around R_{Front}=$1.5 \cdot R_{Turb}$. Consequently, both values would indicate that the R_{Front} could be slightly increased.

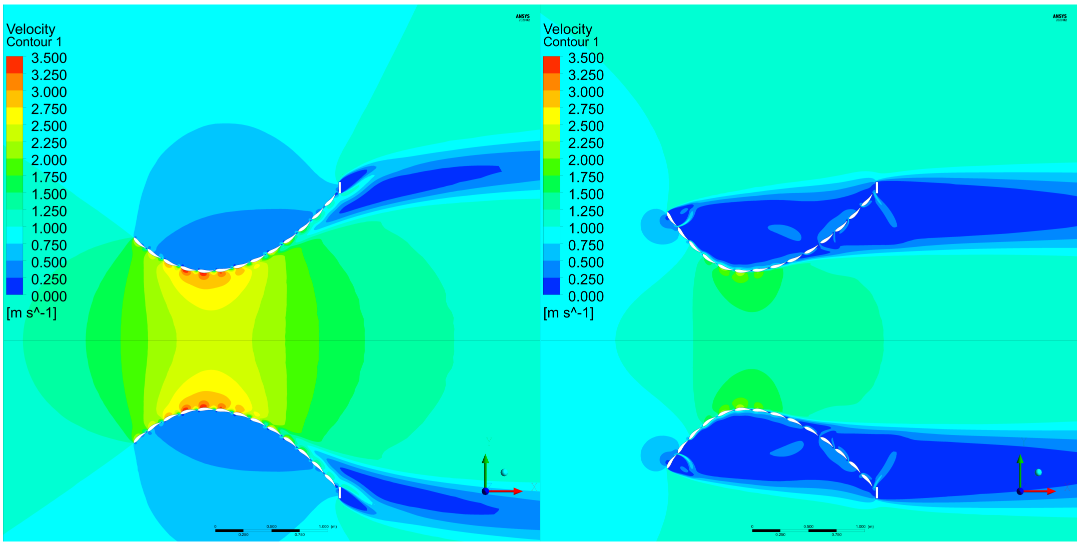

Figure 6. Velocity plot comparing R_{Front}=$1.5 \cdot R_{Turb}$ (left) and R_{Front}=$1.8 \cdot R_{Turb}$ (right) with a fixed L_{Front}=$1.1 \cdot R_{Turb}$.

As shown in Figure 6, a velocity drop occurs due to recirculation zone changes. A larger R_{Front} value results in the side structure acting like a blockage and reducing the flow speed inside to near zero. Consequently, this is not only influenced by the nozzle but also of the diffusor, including the brim as well as the flow speed. In the case of the larger R_{Front} (Fig. 6 right), a leakage of the flow behind the first hydrofoil is obvious, which indicates that this combination does not guide the flow as intended.

The main conclusion, which can be drawn based on this variation assessment, is that the inlet dimension of the reference geometry is in a satisfactory range. The parameter R_{Front} is critical but an expansion close to or even beyond the outlet R_{Back} results in no further improvements. Such a drop must be prevented and the final design should tolerate some uncertainty to stay in the correct flow regime.

3.3. Variation of the diffusor including brim

The variation of the nozzle part of the Venturi structure indicated that the diffusor section should reach further out in the orthogonal direction as the front part. Consequently, smaller R_{Back} values are excluded and larger steps for the variation of 360 mm ($0.6 \cdot R_{Turb}$) are investigated. Figure 7 provides an overview similar to Figure 5, which is described in Section 3.2. Similarly to the front, the parameter R_{Back} has a more significant influence than the length L_{Back}. An increase of R_{Back} not only directly enhances the average velocity at the turbine section $\overline{vel}_c$ but also the intensify the total forces acting on the structure. It has to be highlighted that the increase from

2.5 m/s to close to 3.25 m/s with the larger R_{Back} results in scaled forces, multiplied by a factor of about 8.

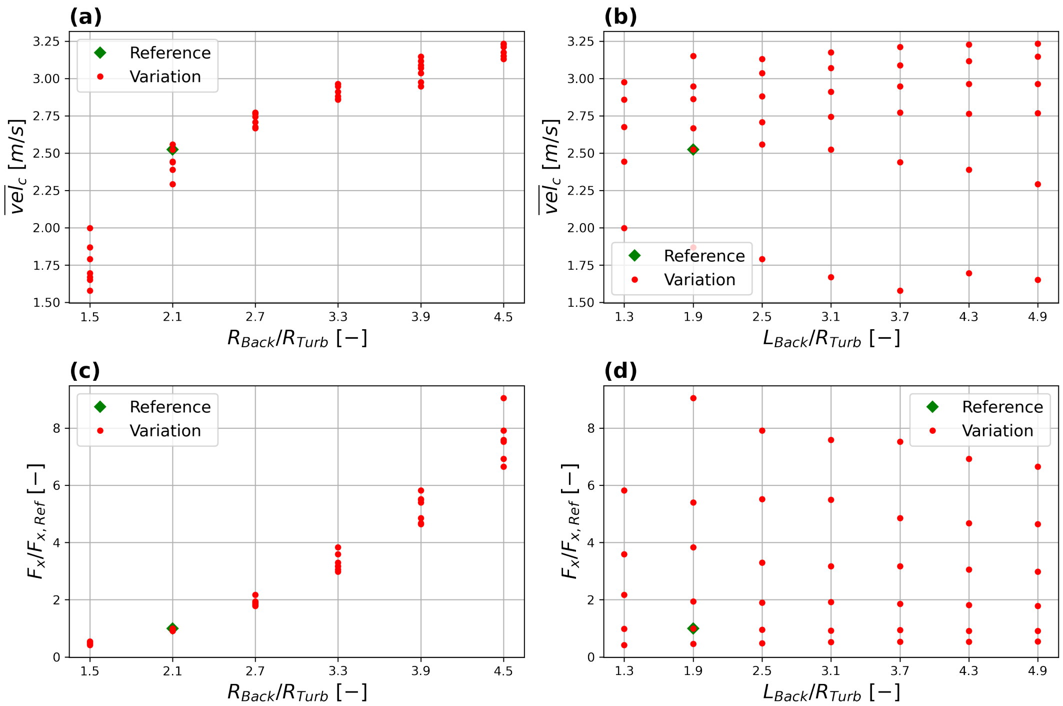

Figure 7. Variation of the diffusor with a fixed nozzle $[R_{Front}, L_{Front}] = [1.2, 1.1] \cdot R_{Turb}$ — area-averaged velocity at the turbine cross section $\overline{vel}_c$ depending on the opening radius R_{Back} (a) and sorted by the length L_{Back} (b) — Forces in x-direction F_x standardised by the reference value (c-d) — all length standardised by the turbine radius R_{Turb}.

Hence large R_{Back} act similar to a brim, the result effects of including this additional blockage element are described within this section. Starting from the reference geometry, which is presented in Section 2.4, the length of the additional brim is changed, results of which are presented in Figure 8. With an initial R_{Back} of $2.1 \cdot R_{Turb}$, the brim reaches out further $2.4 \cdot R_{Turb}$ and consequently covers a blockage of $4.5 \cdot R_{Turb}$, which is similar to the maximum expansion of the geometry parameter R_{Back} of the diffusor (Fig. 7). An increasing h_{Brim} causes a direct increase of the indicator $\overline{vel}_c$ at the turbine cross section but also a significant increase of the forces F_x acting on the overall structure. The conducted variation of the h_{Brim} indicates that the velocity converges in the range of 3.2 m/s, while the forces are increased by a factor of 8. This is very similar to the variation of the R_{Back} and explains why both parameters are detailed jointly within this section. Clearly, the optimisation of both parameters is not driven by the hydraulic characteristic but instead by construction costs.

Figure 9 presents the extreme cases for the variable R_{Back} with the shortest length L_{Back}. The geometry with the largest R_{Back} introduces a massive blockage and acts more like a brim with holes. Based on the literature (Nunes et al., 2020), an inclination of the brim to the front instead of to the back might be advantageous. The observed convergence behaviour of the simulation with more extreme values indicates that the flow is not longer steady state and a transient solver would be more appropriate. This is also obvious in the Figure 9 (right), which shows that the downstream jet is slightly orientated in the positive y-direction, indicating flow instability caused by this extreme values of the diffusor part of the geometry.

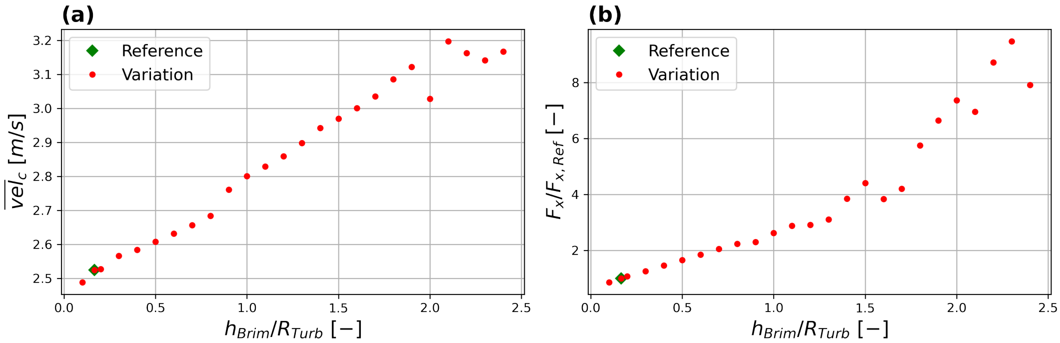

Figure 8. Variation of the height h_{Brim} of the additional brim — area-averaged velocity at the turbine cross section $\overline{vel}_c$ (a) and Forces in x-direction F_x standardised by the reference value (b) — all length standardised by the turbine radius R_{Turb}.

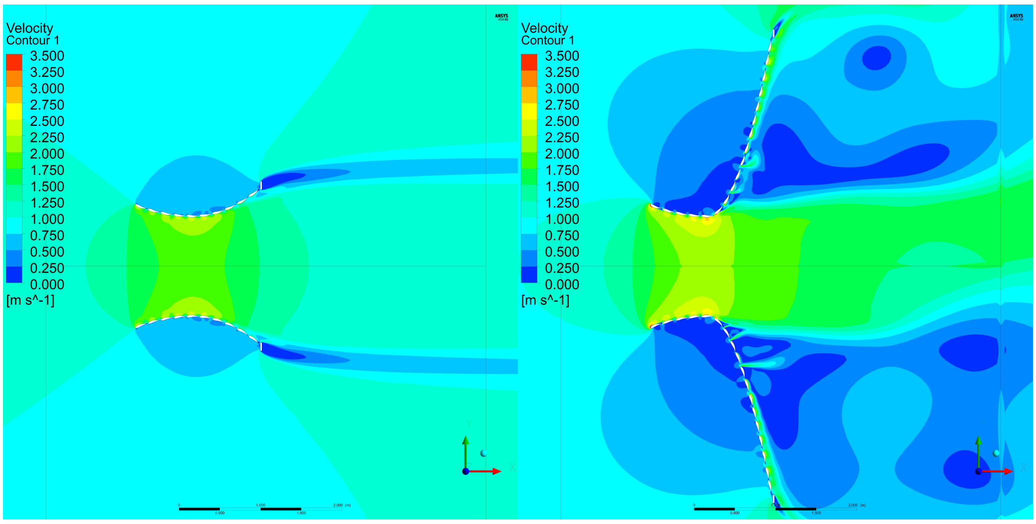

Figure 9. Velocity plot comparing R_{Back}=1.5 · R_{Turb} (left) and R_{Back}=4.5 · R_{Turb} (right) with a fixed L_{Back}=1.3 · R_{Turb}.

An expansion of the R_{Back} as well as the h_{Brim} results in not only higher velocities but also increased forces. The extreme expansion of R_{Back} can be combined or even replaced with a larger brim, which might be more cost effective than the hydrofoils. But for a real application the additional loading will be prohibitive if too large values are chosen. An addition of a second turbine instead of a single large turbine should be considered in this case.

3.4. Variation of the turbine radius

For all previously reported variations of the geometry the turbine radius R_{Turb} is set to 600 mm, which is used as the reference value $R_{Turb,Ref}$ for the following variation of this parameter. Two different concepts of the variation are investigated: (a) the dimension R_{Turb} is varied independently of the other parameters (Figs. 10 and 11) and (b) the change of the R_{Turb} is similarly applied for the other two length in the y-direction of the geometry. The latter results in a parallel movement of the reference geometry reducing or widening the middle cross section (Figs. 12 and 13).

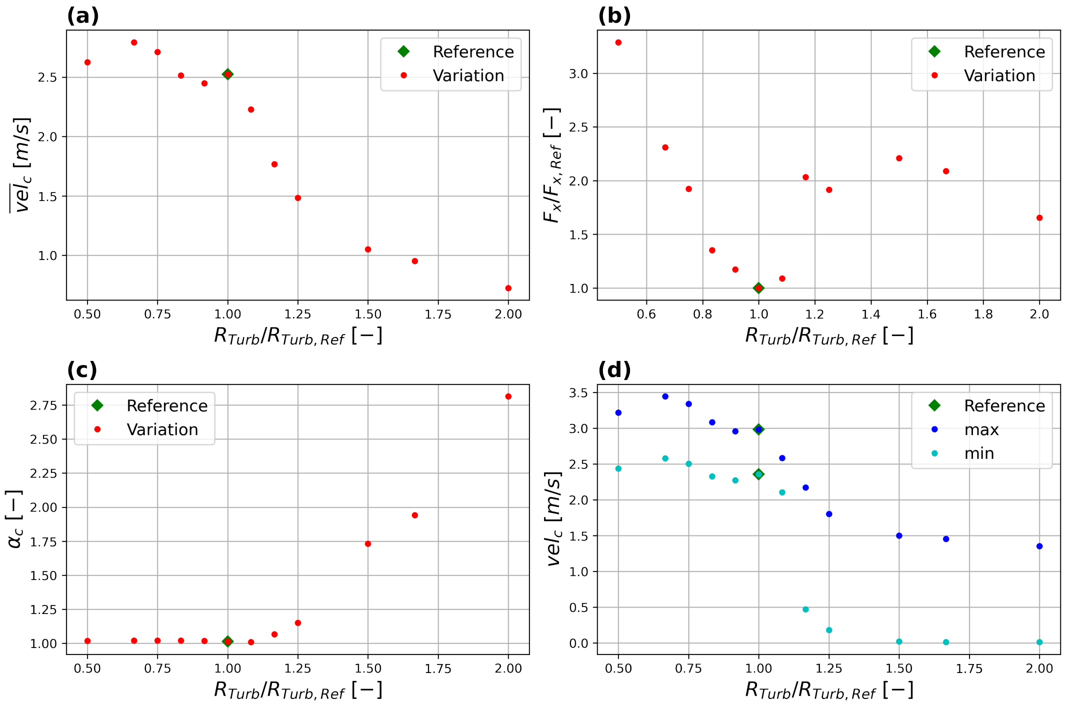

Figure 10. Variation of the turbine radius R_{Turb}, while all other geometry parameters are kept to the reference values — area-averaged velocity at the turbine cross section $\overline{vel}_c$ (a), forces in x-direction F_x standardised by the reference value (b), kinetic energy flux coefficient α_c for the turbine cross section (c) and the extreme values of the velocities in the turbine cross section (d) — all length standardised by the turbine radius of the reference geometry $R_{Turb,Ref} = 600$ mm.

The independent variation of the turbine radius R_{Turb} is added more for completeness and not for their actual usability within the optimisation. Since the possibility to install the turbine is not specifically checked, these cases are not realistic. For those simulations, the inlet dimension of the nozzle were fixed with $R_{Front} = 1.2 \cdot R_{Turb,Ref}$ and consequently all R_{Turb} values, which exceed this length, the complete flow regime changes. Figure 10 shows that for larger R_{Turb} values the $\overline{vel}_c$ is significantly reduced. This results in flow speeds under 1 m/s (boundary conditions at the inlet), which would be worse than having no supporting structure. The analysis of the α_c indicates an extreme increase of inhomogeneous flow and the minimum value of the velocity falls down to 0 m/s. Such an expansion is clearly not a good choice. Figure 11 clearly show that the recirculation zone moves from the outside to the inner area, which is far from a favourable result.

More realistic than the previously single variation of the R_{Turb} is a parallel change of the structure. Where all parameters in the y-direction, namely R_{Turb}, R_{Front} and R_{Back}, are change with the identical value. This results in a constant offset in the y-direction keeping the geometry symmetrical to the x-axis. The results of this variation are presented in Figure 12 covering a range of a quarter of the initial reference radius to the doubled value. Reducing the space between the side Venturi structures increases the average velocity at the turbine cross section $\overline{vel}_c$ but also results in a higher total force F_x on the structure. Reducing R_{Turb} to $0.25 \cdot R_{Turb,Ref}$ increases flow speed in the range of additional 1 m/s while also multiplying the resulting forces by a factor of

2.5 in relation to the reference values with a $R_{Turb,Ref} = 600$ mm.

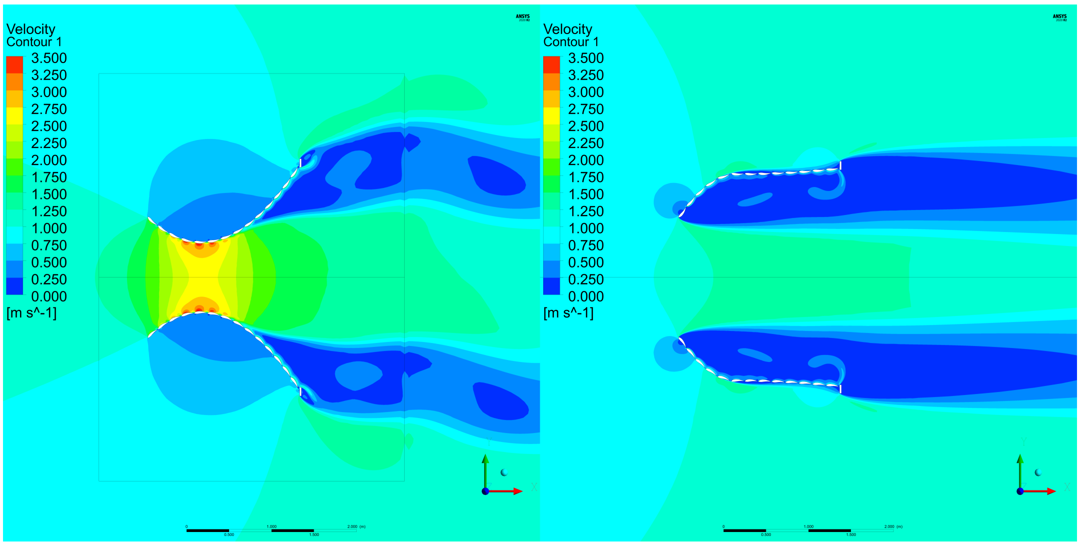

Figure 11. Velocity plot comparing the reference geometry with a turbine radius R_{Turb} of 400 mm, which is equal to $0.66 \cdot R_{Turb,Ref}$ (left,) in comparison with $2 \cdot R_{Turb,Ref}$ (right).

The velocity distribution becomes more homogeneous with the a smaller R_{Turb} indicating by the α_c-value and a comparable small velocity difference of 0.5 m/s (maximum subtracted by the minimum velocity). In this case the cross section at the turbine is reduced to a quarter but the discharge, which flows through the cross section reaches approximate 34% of the discharge through the reference geometry.

The smallest investigated distance between both sides is compared with the largest configuration in the Figure 13. It shows the comparable high velocity in the turbine cross section, which results in a jet at the outlet. The obvious asymmetry of the velocity distribution in the wake of the turbine indicates that an unstable flow is generated. It seems that each side has a range of influence and if the distance in reduced, both sides support each other. To test this assumption, a specific variation of the full structure is presented in Section 3.5. In any case, this investigation has to be repeated in a full 3D-model and with a full turbine model in order to assess if higher velocities can generate a positive impact on energy production.

This section includes a theoretical investigation of the single variation of the turbine radius R_{Turb}, which resulted in some completely different flow regimes. The second variation proposes a parallel offsetting of both side geometries with the scaling of all three defining lengths in the y-direction. Narrowing the channel between both sides resulted in increased velocities and forces. This indicates that a combined variation of nozzle and diffusor have the potential to improve the velocity at the turbine further. How far this is beneficial for the actual energy production at the turbine will need to be investigated separately.

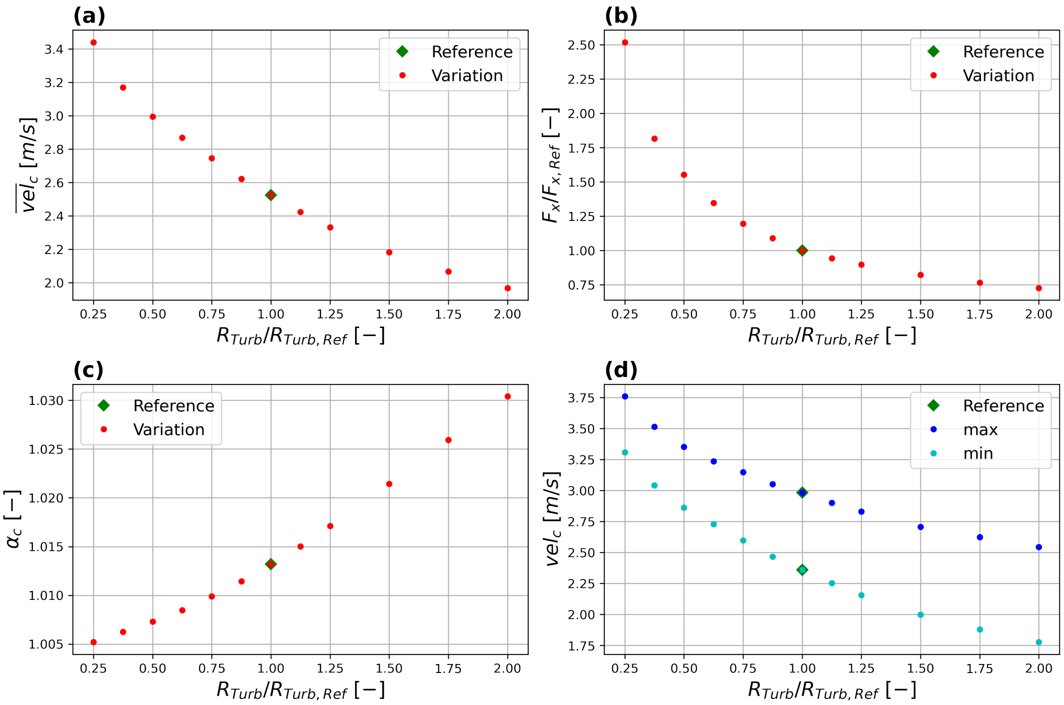

Figure 12. Variation of the turbine radius R_{Turb} including R_{Front} and R_{Back} resulting in parallel move of the sides — area-averaged velocity at the turbine cross section $\overline{vel}_c$ (a), forces in x-direction F_x standardised by the reference value (b), kinetic energy flux coefficient α_c for the turbine cross section (c) and the extreme values of the velocities in the turbine cross section (d) — all length standardised by the turbine radius of the reference geometry $R_{Turb,Ref}$ = 600 mm.

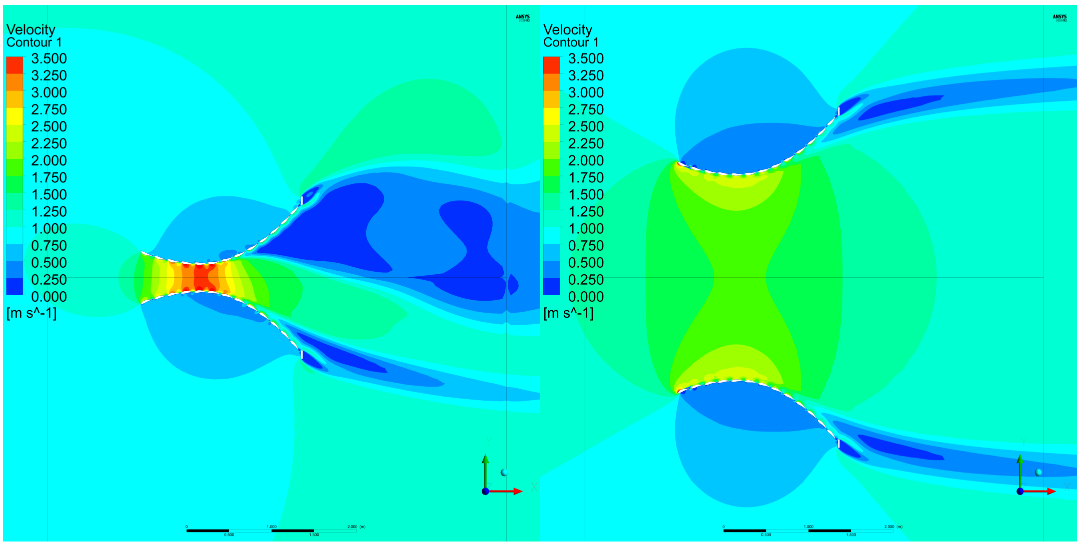

Figure 13. Velocity plot comparing two cases with a parallel move of the structure with the turbine radius R_{Turb}: $0.25 \cdot R_{Turb,Ref}$ (left) and $2 \cdot R_{Turb,Ref}$ (right).

3.5. Combination – scaling the structure

The second part of the previous Section 3.4 shows that a parallel offsetting of the full structure to the centre results in increased speed at the centre of the turbine (Fig 12). A preliminary hypotheses is the aforementioned range of influence one side has to the other, which overlaps if the sides are close enough. To test this, a combined change of the nozzle and diffusor part is investigated in this section. The factor fac is used to scale the geometry while keeping the turbine radius R_{Turb} constant. This factor is applied directly to the length L_{Front} and L_{Back} as well as to the difference value of the R_{Front} and R_{Back} as presented in Eq. (3).

$$fac = \frac{L_{Front}}{L_{Front,Ref}} = \frac{L_{Back}}{L_{Back,Ref}} = \frac{R_{Front} - R_{Turb}}{R_{Front,Ref} - R_{Turb}} = \frac{R_{Back} - R_{Turb}}{R_{Back,Ref} - R_{Turb}} \tag{3}$$

This is obviously not perfectly scaled since the hydrofoils remained one type, maintaining specific lengths and distances along the channel, but it does provided an approximation allowing the simulation of comparable geometry changes as conducted with the variation of the R_{Turb} (Fig. 12). The results of this scaling are shown in Figure 14. A smaller factor fac down to 0.5 is comparable to a larger R_{Turb} (larger distance between the two sides). Both result in a reduction of the velocity at the turbine cross section $\overline{vel_c}$ and the total forces F_x. A variation in the other direction shows similarity with the previously reported $R_{Turb}/R_{Turb,Ref} = 0.5$ (Fig. 12) a $\overline{vel_c}$ of approximately 3 m/s, which can also be found for a scaling factor $fac = 2$ in Figure 14. This indicates that both geometries are comparable, however, the forces show that $R_{Turb}/R_{Turb,Ref}$ equates to 1.5 times (Fig. 12) of the reference value, while it is 2.5 times (Fig. 14) the loading for the scaled version of the geometry. This scaled geometry has a $R_{Back} = 3.2 \cdot R_{Turb,Ref}$ and $L_{Back} = 3.8 \cdot R_{Turb,Ref}$. Although comparable in geometry, with the front section fixed to the reference geometry, the results show $\overline{vel_c}$ of around 3 m/s with higher ratios of $F_x/F_{x,Ref}$ greater than 4 (Fig. 7). The analysis in Figure 14 also includes a further adaptation for the extreme values while only the R_{Front} and R_{Back} is modified by the factor fac. For those two specific cases, the lengths L_{Front} and L_{Back} are kept at the reference length (Sec 2.4). This was completed in Section 3.2 and 3.3 which identify the R-dimensions as dominate parameters. The direct comparison to the values for the full scaling with a factor fac of 0.5 and 2 show, that those specifically marked parameters result in a lower $\overline{vel_c}$, higher F_x, comparable α_c-values and the range of the extreme values is wider and moved. Consequently, full scaling shows better results than utilising only R-scaling.

Figure 15 shows the velocity plots of the four mentioned extreme values. The two top row pictures present the results of the full scaling according to the Eq. (3). For the geometries in the bottom row, lengths L_{Front} and L_{Back} are not scaled and only R_{Front} and R_{Back} are. These results indicate that the R-length in the geometry are dominate but that scaling in length along the flow direction should also be considered. How far such an adaptation results in a real performance improvement must be checked separately.

3.6. Angle of the first hydrofoil

This specific section focuses on the orientation of the first hydrofoil in the flow direction, describing a key function which provides the addition of an initial direction

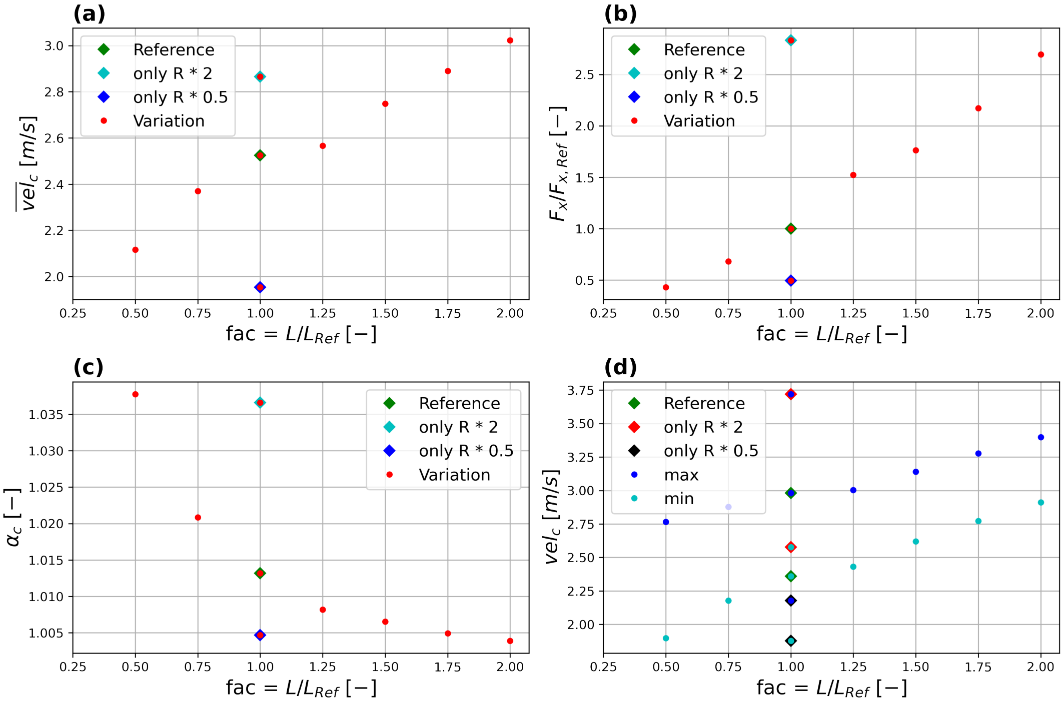

Figure 14. Scaling by different factors f of the structure with a fixed turbine radius R_{Turb} — area-averaged velocity at the turbine cross section $\overline{vel}_c$ (a), forces in x-direction F_x standardised by the reference value (b), kinetic energy flux coefficient α_c for the turbine cross section (c) and the extreme values of the velocities in the turbine cross section (d).

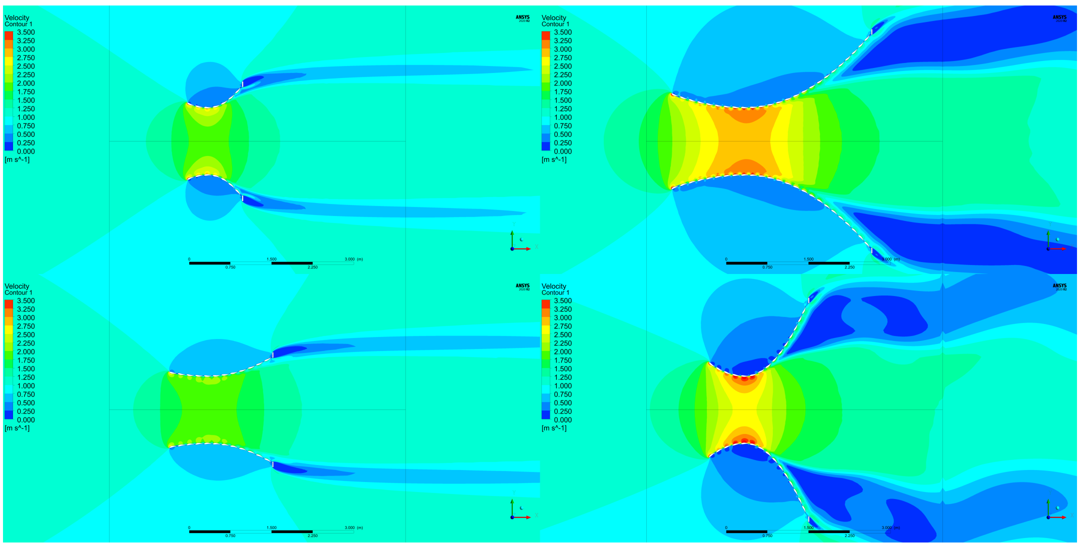

Figure 15. Velocity plot comparing four different scaled geometries: factor fac =0.5 (left,top) and 2 (right, top) — the scaling is only applied for the R-values with a fac = 0.5 (left, bottom) and 2 (right, bottom).

change included to benefit of the Venturi structure. The parameter $\Delta\alpha_{FirstFoil}$ is introduced to describe this additional angle of this specific foil. For all other cases, the hydrofoil is rotated according to the tangential direction of the bell shape at the definition point of the individual hydrofoil.

The conducted variation of this additional angle covers a range of $\pm 90°$ from the original tangential orientation with a $\Delta\alpha_{FirstFoil} = 0°$. Figure 16 presents the results, showing that incremental negative angles improve the area-averaged velocity at the turbine cross section $\overline{vel_c}$ occurring at velocities slightly over 2.6 m/s around a $\Delta\alpha_{FirstFoil}$ of -20°. This is also connected with a reduction of the total forces in the x-direction. Consequently, such a modification of the first hydrofoil is advantageous.

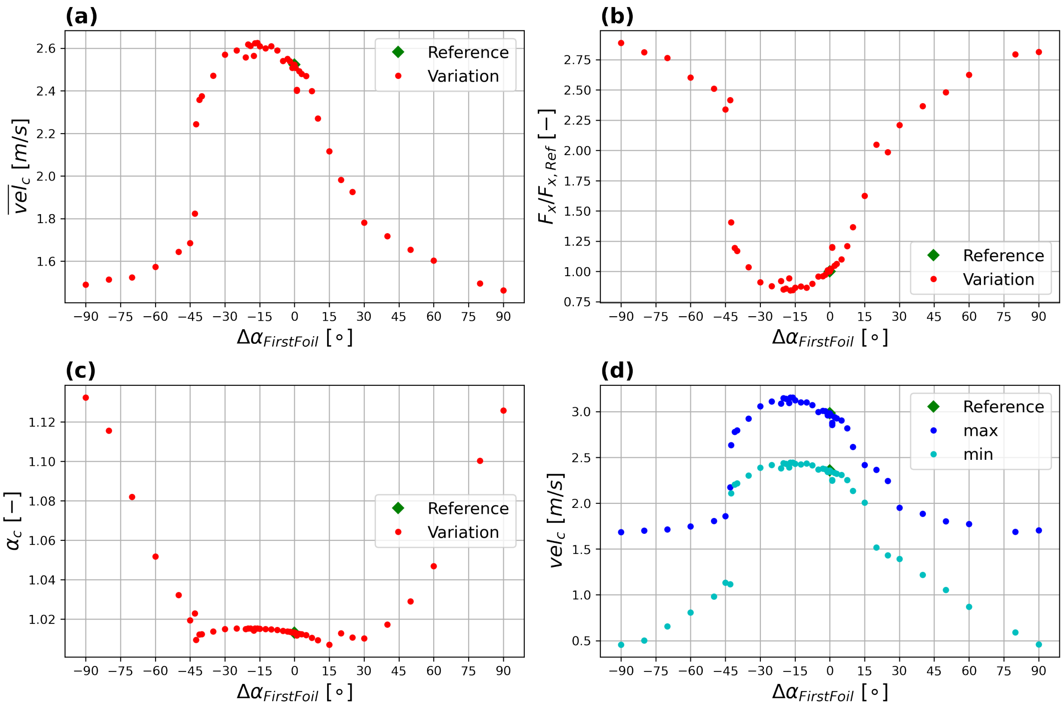

Figure 16. Variation of the additional angle of the first hydrofoil $\Delta\alpha_{FirstFoil}$ — area-averaged velocity at the turbine cross section $\overline{vel_c}$ (a), forces in x-direction F_x standardised by the reference value (b), kinetic energy flux coefficient α_c for the turbine cross section (c) and the extreme values of the velocities in the turbine cross section (d).

The conducted variation of the parameter is deliberately expanded to investigate the range of influence in more detail. Extreme values of $\pm 90°$, for example, result in a significant reduction of the velocity value $\overline{vel_c}$, while the kinetic energy flux coefficient α_c is significantly increased. This indicates that the first hydrofoil introduces a disturbance, which has a downstream influence. Obviously, this can also be seen in the evaluation of the extreme values in the turbine cross section shown in Figure 16 (d). Minimum values are reduced to 0.5 m/s, equal to half of the inlet velocity of 1 m/s.

Figure 16 indicates that an optimum value can be reached by including an additional angle of around -20°. The benefits are presented in the top row of Figure 17. A value of -20° for the parameter $\Delta\alpha_{FirstFoil}$ results in the end of the first hydrofoil being placed slightly closer to the symmetry plane (x-z-plane) leading to an overall flow velocity increase. A rotation in the opposite direction generates a step and the flow detaches. The ramification of which is an overall reduced flow speed at the turbine cross section as well as higher forces on the structure. The extreme values of $\pm 90°$ are also shown in the Figure 17 representing the boundaries of this variations. Both cases are obviously not ideal.

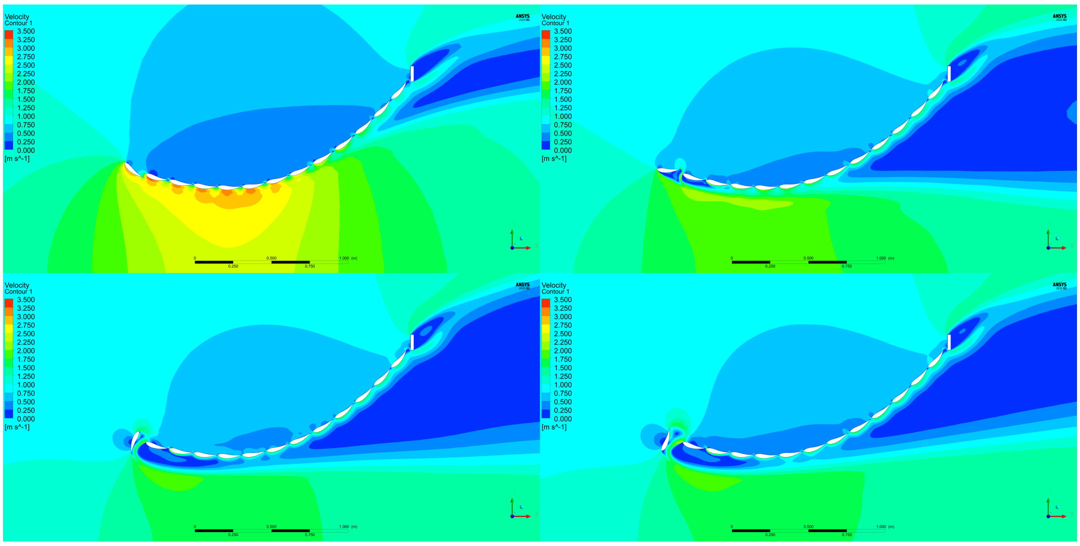

Figure 17. Velocity plot comparing four different additional angles applied on the first hydrofoil in the flow direction: $\Delta\alpha_{FirstFoil}$ =-20° (left,top), 20° (right, top), -90° (left, bottom) and 90° (right, bottom).

The orientation of the first hydrofoil in the flow direction has a significant influence, while the precise optimum angle is dependant on the size and type of hydrofoil profile implemented. Consequently, this parameter is one of the last criteria to optimise after key geometry decisions are made.

3.7. Hydrofoil length and distance

The previous variation focused on the main component of the geometry utilising a single hydrofoil GOE 222 (MVA H.33) AIRFOIL (Airfoil Tools, 2022) with a chord length c_{Foil} of 150 mm and a linear chord distance s_{Target} of 160 mm between the definition point of each hydrofoil on the bell curves. The type of the hydrofoil is varied in Section 3.8 and this section focuses on the length as well as the distance between the foils.

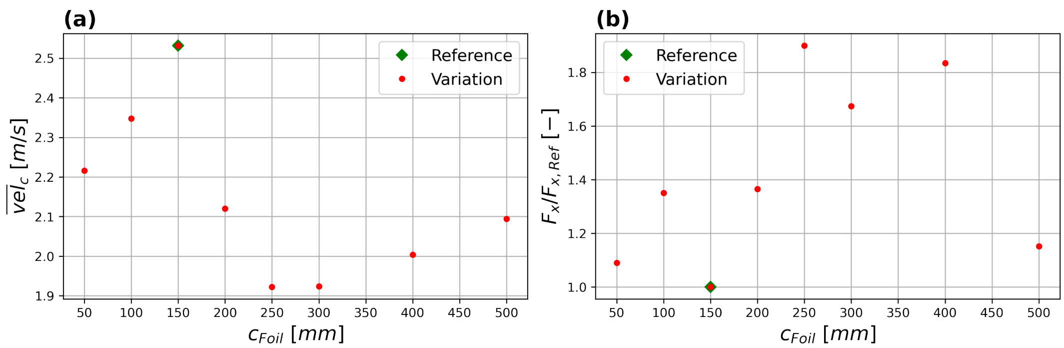

Figure 18. Variation of the chord length c_{Foil} of the hydrofoil — area-averaged velocity at the turbine cross section $\overline{vel}_c$ (a) and Forces in x-direction F_x standardised by the reference value (b).

Figure 18 shows the results for different chord length of the same standard hydrofoil. A range between 50 mm and 500 mm is presented. The smaller blades use the same concept for the calculation with $s_{Target} = c_{Foil} + 10$ mm, while additional values were increased to 20 mm for the 400 mm foil and 30 mm for the 500 mm foil. This ensured that the individual elements are separated. Looking only at this analysis, the average velocity at the turbine section $\overline{vel}_c$ is maximised and the forces F_x are at a low level (Fig. 18). The four examples shown in Figure 19 indicated that the choice of the blade size has a significant influence on the structure.

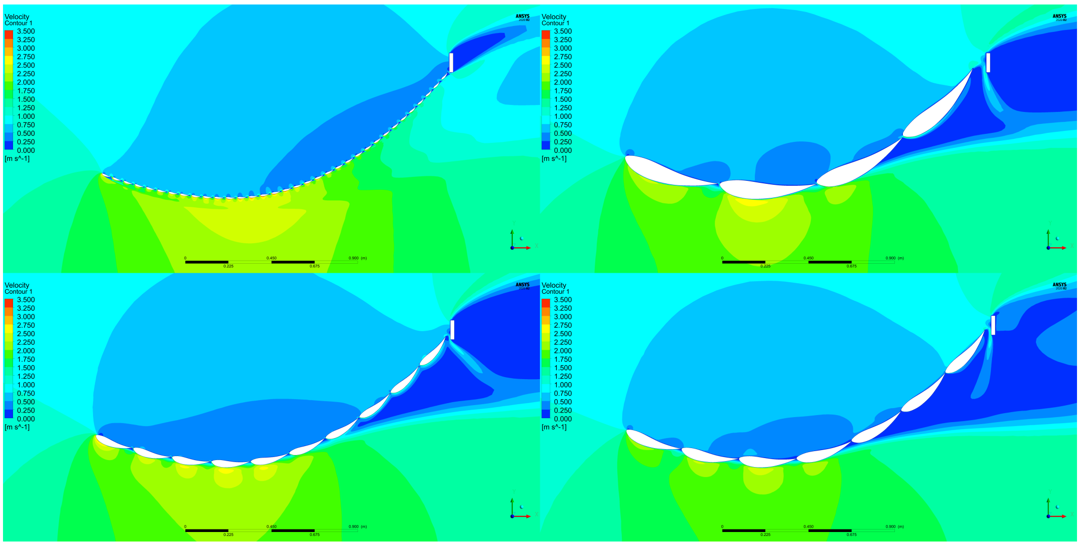

Figure 19. Velocity plot comparing four different length of the hydrofoil: 50 mm(left,top), 200 mm (left, bottom), 300 mm (right, bottom) and 500 mm (right, top).

The previous sections show that specific parameters can have a significant influence on the overall performance of the turbine. It also must be noted that the definition point of all cases is identical but the bell shape can only be filled with the same hydrofoils based on the constant linear chord distance along the curves. Smaller profiles can better reach a precise endpoint and the larger profiles would have to be spaced perfectly to reach a better comparability. Keeping the limitation of this comparison in mind, all investigated length performed in a very comparable way and might need more detail optimisation to reach an optimum.

In a second step, the linear chord distance s_{Target} is varied to investigate the initial choice of 160 mm. This is conducted for the hydrofoil GOE 222 (MVA H.33) AIRFOIL (Airfoil Tools, 2022) only, with a chord length c_{Foil} set to 150 mm. s_{Target} is varied between 155 mm and 300 mm, which is double the chord length of the hydrofoil. For this variation the step size Δs is changed from 10 mm to 1 mm to better represent the small alterations of the parameters within each simulation. This value is used to find the required x-distances for the following definition point, indicating that these changes result in a reduction of the $\overline{vel}_c$ for the reference geometry. Consequently, for this case, two variation points are reported in Figure 20 for the s_{Target} length of 160 mm. A slight expansion results in an overall improvement of the $\overline{vel}_c$ and reduction of the total forces F_x can be observed, with an optimum point at 166 mm. It is not surprising, that larger values introduce large gaps in the structure and hence the efficiency is reduced. Figure 21 shows the comparison of the a s_{Target} of 166 mm and the largest value of 300 mm. With a larger gap between the individual hydrofoils the behaviour of the structure changes from a joint guidance of the flow into separate obstacles in the flow.

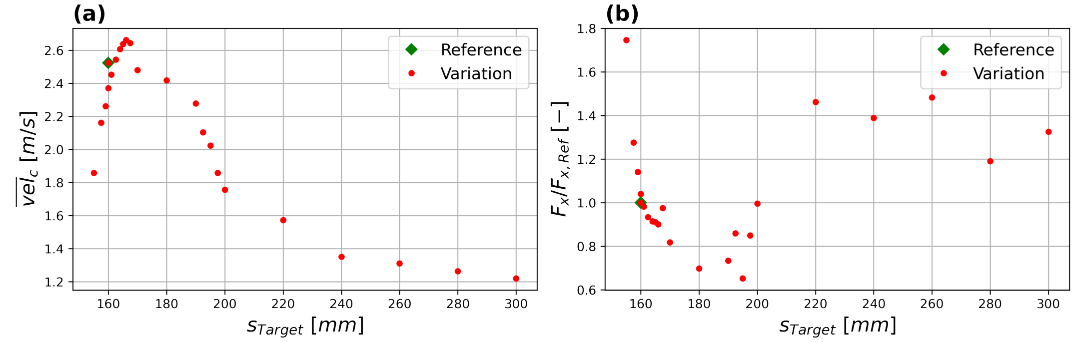

Figure 20. Variation of the length s_{Target}, which defines the distance between the reference points on the bell shape — area-averaged velocity at the turbine cross section $\overline{vel}_c$ (a) and Forces in x-direction F_x standardised by the reference value (b).

This variation of hydrofoil chord length and the definition point indicates that the initial chosen values are in a good range. Nevertheless, the distance between the definition points of the hydrofoils indicated some optimisation potential. However, extremes in hydrofoil sizing do not provide better results. The decisive point for this decision is more the likely the availability and costs of the production of the hydrofoils.

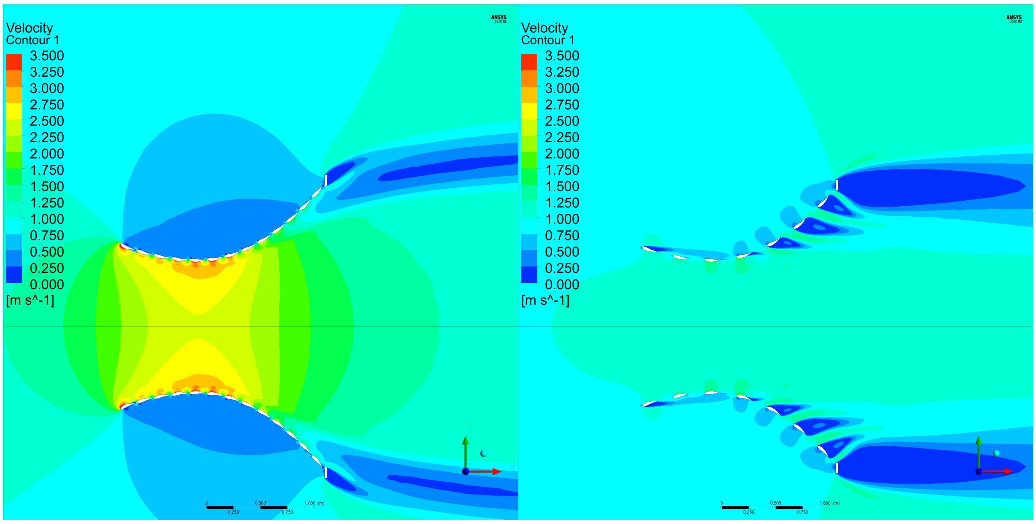

Figure 21. Velocity plot comparing two different chord length s_{Target} between the definition points of the hydrofoils: 166 mm(left) and 300 mm (right).

3.8. Hydrofoil type

In this section the type of hydrofoil is altered, while keeping a constant chord length $c_{Foil} = 150$ mm and distance between the definition points for the individual foils $s_{Target} = 160$ mm. Similar to the GOE 222, the geometry data is sourced from the online database Airfoil Tools (2022), which provides over 1600 different airfoil types. The selection of additional foils were conducted based on a random choice, while trying to cover a wider range of different shapes. In addition, a circular cross section is also tested, for which the s_{Target} has to be increased to 165 mm (Note that for this simulation the definition points are located on the inside of the turbine and not in the centre line of the hydrofoils). Figure 22 provides an overview of the investigated types.

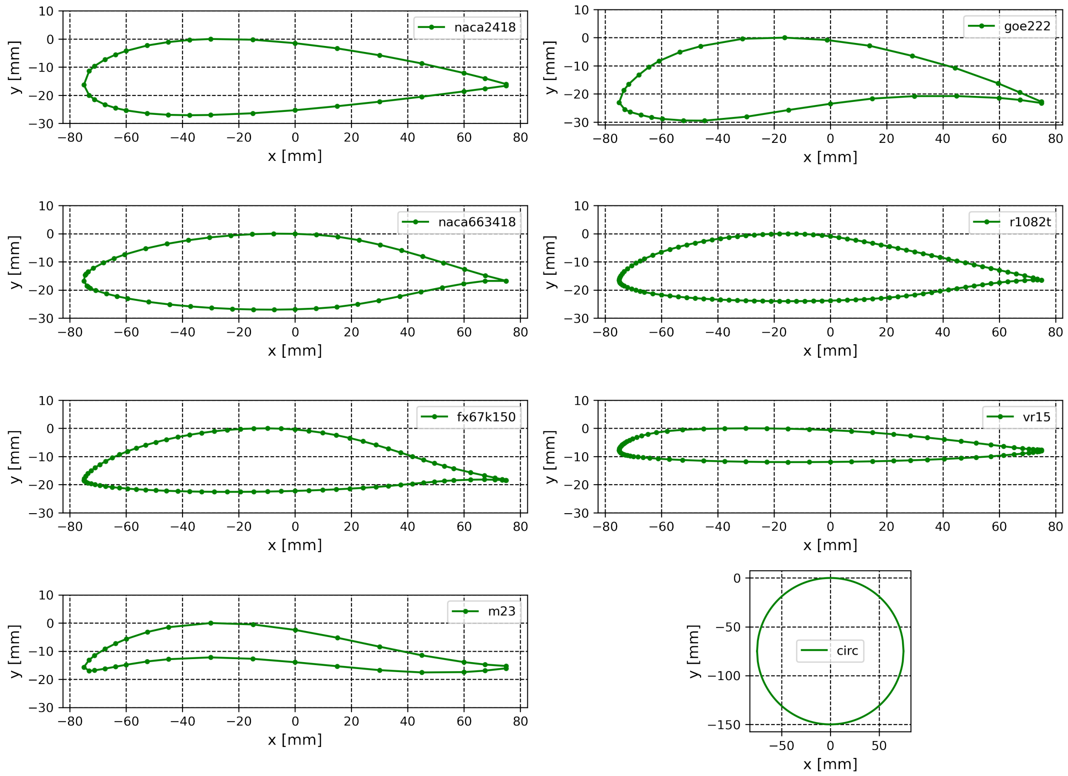

Figure 22. Overview of the investigated hydrofoils.

The results of the variation of the hydrofoil types is presented in Figure 23, sorted depending on the area-averaged velocity at the turbine cross section $\overline{vel}_c$. A slight improvement in velocity as well as the total forces in the x-direction is noted with the NACA 2418 hydrofoil. All other foils resulted in worse conditions with a massive reduction for the circular cross section. The latter requires a much more massive structure while only producing a slightly higher total force. The kinetic energy flux coefficient α_c is very similar for all investigated hydrofoils with the largest inhomogeneity shown for the circular profile, which provides the most extreme values for the velocities in the cross section.

Figure 24 shows the comparison of four of the eight investigated options. The top row shows the best and worst options side by side and it is obvious that the circular cross section is not a good option for this approach. The comparable large radius of the circle in the lateral direction result in a comparable massive structure and it works

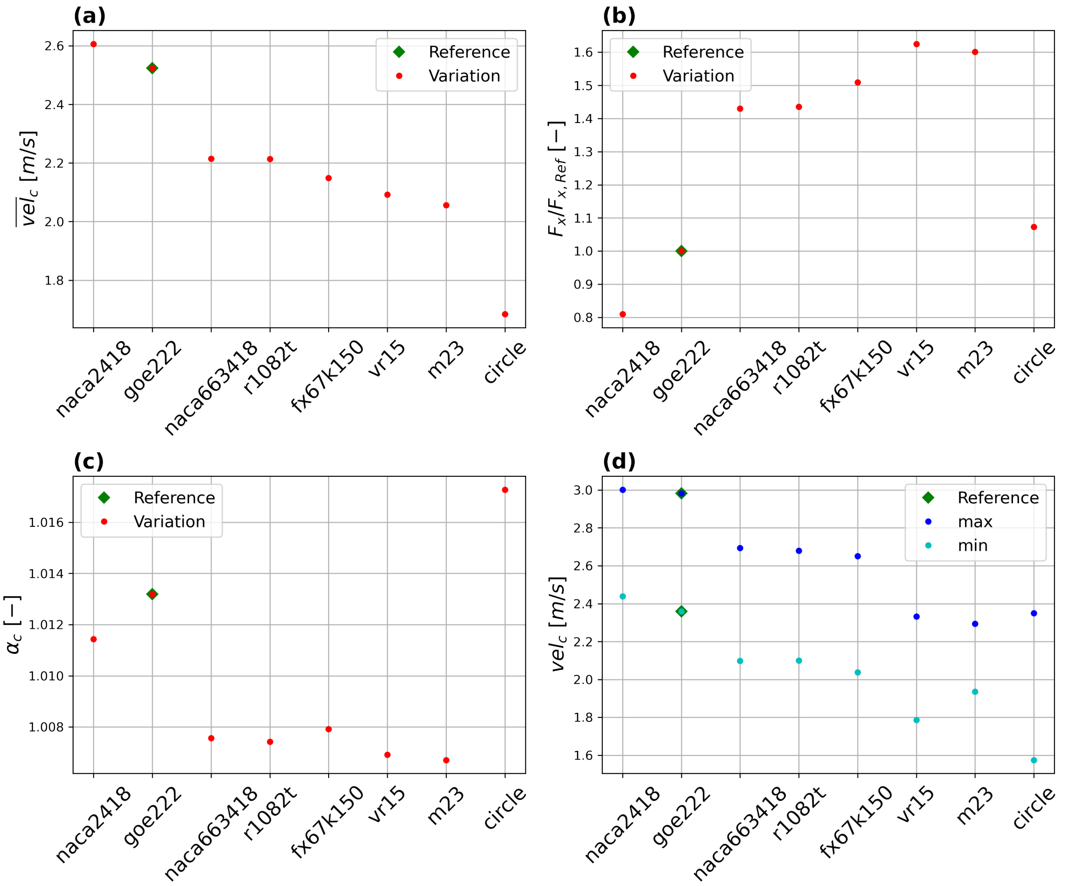

Figure 23. Variation of the hydrofoil types — area-averaged velocity at the turbine cross section $\overline{vel}_c$ (a), forces in x-direction F_x standardised by the reference value (b), kinetic energy flux coefficient α_c for the turbine cross section (c) and the extreme values of the velocities in the turbine cross section (d).

more like a solid Venturi channel with additional wall roughness. Interestingly the tip of the foil of the very thin M23 hydrofoil. The flow detaches very early and results in a small recirculation zone behind the first foil. On the other hand, the two foils on the left cause a velocity peak at this location. This indicates that the fixed angle along the bell curve with an orientation along the tangential direction is not ideal for all foils. A correction of the first foil in the incoming flow direction could result in an improvement of the results for this specific foil.

This section analyses seven additional hydrofoils for comparison with the originally used GOE 222 foil. Slight improvement can be found changing to a NACA 2418, which is more symmetric and has the potential to be less expensive for manufacture. The distance between the definition points of the hydrofoils may allow for further improvements, such as that shown in Section 3.7. Importantly, it was found that the orientation of the first foil in the flow direction is critical, and hence a correction angle for this specific profile was added in the Python code for the generation of the geometry in Gabl et al. (2022) and a variation is presented in Section 3.6.

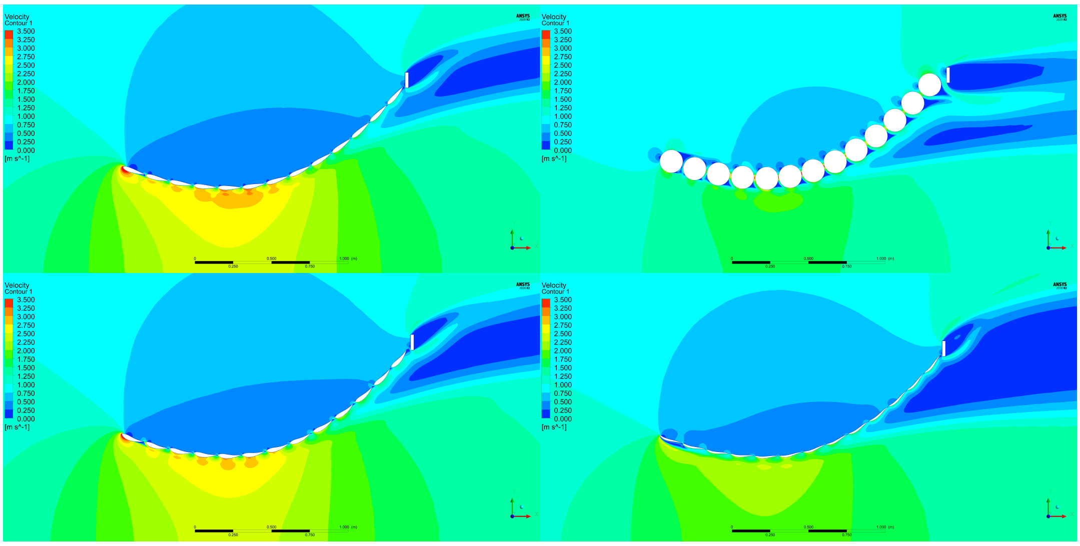

Figure 24. Velocity plot comparing the reference geometry with three other types of hydrofoils: NACA 2418 (left,top), GOE 222 (left, bottom), M23 (right, bottom) and circle (right, top).

3.9. Inlet velocity

All previous simulation assumed that the inlet velocity is constant 1 m/s, which is introduced homogeneously at the inlet boundary conditions. In this section, the value is varied over a range of 0.5 to 2 m/s, while keeping all the other assumptions the same, including the constant reference geometry (Sec 2.4). Figure 25 presents the results of this variation. Contrary to the previous analysis, the velocity at the turbine cross section $\overline{vel}_c$ is normalised by the inlet velocity v_{Inlet}. Hence the standard v_{Inlet} is 1 m/s, the values can be directly compared with the previous results, while being non-dimensionalised. This value changes in relation with v_{Inlet} in a range of approximately $\pm$ 0.2 [-] from the reference value. A doubling of the v_{Inlet} causes an increase of the forces by a factor of approximate 3.5 [-]. Tidal flows are generally very predictable but nevertheless extreme flow speeds can occur resulting in extreme loads on the structure.

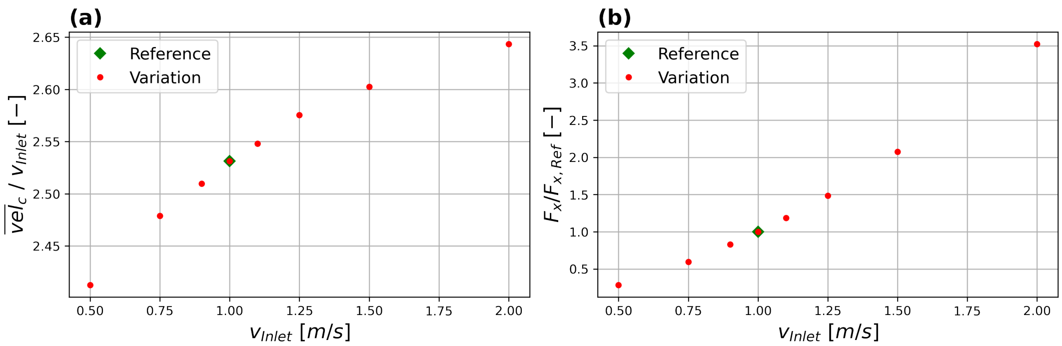

Figure 25. Variation of the inlet velocity v_{Inlet} to investigate the standardised velocity at the turbine cross section $\overline{vel}_c$ (a) and the total forces F_x on the structure in x-direction (b).

Figure 26 provides the slowest and fastest investigated flow speeds of 0.5 and 2 m/s respectively. A separate colour bar is used for each result, with maximum values scaled provided according to the inlet velocity. The downstream section with close to 0 m/s is smaller for the increased flow speed. A higher gradient in the cross section can be observed for the higher speed, which can also be seen in an increased normalised $\overline{vel}_c/v_{Inlet}$ value.

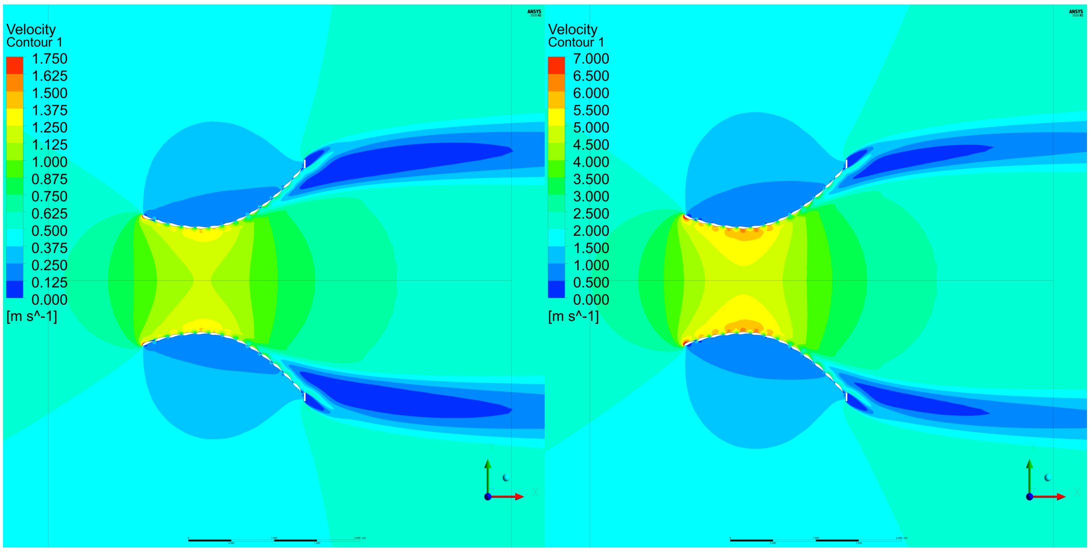

Figure 26. Variation of the inlet velocity v_{Inlet} with 0.5 m/s (left) and 2 m/s (right) — colour bar scaled with the same factor.

In summary, the change of inlet velocity has an influence on the velocity at the turbine cross section $\overline{vel}_c$ making it necessary to optimise the specific design for each deployment site. Extreme flow speeds also have to be considered in the design of the support structure to ensure the survivable of the device.

4. Discussion

The obvious limitation of this presented work is that the numerical simulations are limited to a 2D-approach. All the used computation meshes have only one cell in the vertical direction and hence assuming that there is no change in the z-direction. This neglects potential velocity differences, which are significant closer to the ground Ahmed et al. (2017); Badshah et al. (2018); Ke et al. (2020). Furthermore, the structure has a clear top an bottom part, which is in the previous tests a plane cross section (Fig. 1 (a)). This causes additional interactions and has to be included in the overall optimisation.

It is assumed that the current direction is perfectly aligned, homogeneously distributed and constant. Obviously this is an idealisation and even in deep current streams, the interaction of waves as well as large turbulence in the flow causes variations in the velocity distribution or changes in the flow directions. In all cases, only the steady state solver is used and some results indicated that even with a fully perfect inflow condition the resulting wake can be an unstable flow. The following detailed optimisation has to consider the usage of a fully transient solver.

The computational grid is a standard point, which can be always improved. All current simulations use a comparable fine mesh around the profiles but not a designated inflation layer. Consequently, the y^+- values are comparable high, but similar to comparable investigations (Maduka & Li, 2021) for a further optimisation a designated refinement close to the wall should be considered. The conducted verification process is presented in Section 2.6 but limited to the reference geometry. It is assumed that the mesh independence of the results is also given for changes of the geometry. Section 3 shows that some variations of the geometry cause changes in the location of the recirculating zones and the concentration of the wake in a jet. For those cases, an additional check of the fluid domain and the mesh resolution would be advisable. Nevertheless, those geometries are not likely to be chosen in the future as their performance is not an improvement.

Further limitations can be found in the geometry definition. All cases are built using a single hydrofoil and with identical chord distance set on the bell curves. Hence only full hydrofoils are added, not all changes in the geometry definition have an immediate impact in the actual geometry. A certain threshold has to be exceeded to trigger the addition or removal of a profile. Nevertheless, the conducted geometry generation is ideal for such an exploitative approach but can be refined in an additional detailed optimisation. Furthermore, the hydrofoils are always orientated according to the tangential direction. All of this aspects can be individually modified and varied for each hydrofoil. Obviously, the number of potential options for the investigations increases dramatically.

The presented research work focuses on the Ventrui structure and neglects the influence of the vertical axis turbine. In a following step, the found improvements will be checked, if the changes are really beneficial for the overall energy production. Currently, only fully symmetrical geometries are investigated but there may be benefits in modifying one side, allowing for optimisation of the geometry where the rotating turbine moves against the flow direction. Further detailed investigations are needed to further improve the overall efficiency of the Venturi shaped structure.

5. Conclusions

The presented research work focuses on the hydraulic performance of the surrounding structure of the Davidson Hill Venturi (DHV) tidal turbine. Multiple hydrofoils are placed in a Venturi shape to increase the flow speed at the vertical axis turbine. The first step was to provide a generalised description of the structure (Gabl et al., 2022), which was done in Python allowing future expansions, including using a different numerical solver. In the second step, this geometry description was adapted for the ANSYS-Workbench with the commercial solver ANSYS-CFX, the files for which are available in the connected datashare (Gabl et al., 2022). A wide range of geometry parameters were investigated in a 2D-approach without the turbine based on a reference geometry (Sec 2.4). This variation included the nozzle part as well as the diffusor, including the brim and an additional angle of the first hydrofoil in the flow direction. Larger structures resulted in an improved velocity at the turbine cross section, however, also increased the forces on the structure. The variation of the turbine radius on both sides simultaneously showed potential for further improvements without resulting in extreme operational forces. It can be concluded that the hydrofoil chord length does not significantly influence operational criteria, but that fabrication costs would need to be considered as part of an overall device optimisation. By increasing the gap between the hydrofoils as well as the exchanging the GOE 222 with at NACA 2418 hydrofoil, some improvements in output were shown. In addition to the variations of the geometry, the inlet velocity was varied showing that better results can be achieved with higher flow speeds but no significant decrease for lower speed.

Overall, these variations show that the chosen reference geometry results provide good system performance, with only small improvements being achieved by tweaking design constraints. The next step for the research work is to expand the results from the 2D-approach and integrate the full supporting structure as well as the turbine optimisation.

Disclosure statement

M.H. is the owner of the company, which commercialises the tidal turbine concept presented in this work. The authors declare no further conflict of interest.

Funding

This work was supported by Interreg North-West Europe (NWE) program and the work was carried out as part of the Marine Energy Alliance (MEA) project.

References

Ahmed, U., Apsley, D., Afgan, I., Stallard, T., & Stansby, P. (2017). Fluctuating loads on a tidal turbine due to velocity shear and turbulence: Comparison of cfd with field data. *Renewable Energy*, *112*, 235-246.

Airfoil Tools. (2022). *Online database for the airfoil goe 222.* Retrieved 2022-05-18, from `http://airfoiltools.com/airfoil/details?airfoil=goe222-il`

Alkhabbaz, A., Yang, H.-S., Tongphong, W., & Lee, Y.-H. (2022). Impact of compact diffuser shroud on wind turbine aerodynamic performance: Cfd and experimental investigations. *International Journal of Mechanical Sciences*, *216*, 106978.

Allmark, M., Ellis, R., Lloyd, C., Ordonez-Sanchez, S., Johannesen, K., Byrne, C., ... Mason-Jones, A. (2020). The development, design and characterisation of a scale model horizontal axis tidal turbine for dynamic load quantification. *Renewable Energy*, *156*, 913-930.

Andersson, A. G., Andreasson, P., & Lundström, T. S. (2013). Cfd-modelling and validation of free surface flow during spilling of reservoir in down-scale model. *Eng. Appl. Comput. Fluid Mech.*, *7*(1), 159-167.

Arumugam, P., Ramalingam, V., & Bhaganagar, K. (2021). A pathway towards sustainable development of small capacity horizontal axis wind turbines – identification of influencing design parameters & their role on performance analysis. *Sustainable Energy Technologies and Assessments*, *44*, 101019.

Badoe, C. E., Edmunds, M., Williams, A. J., Nambiar, A., Sellar, B., Kiprakis, A., & Masters, I. (2022). Robust validation of a generalised actuator disk cfd model for tidal turbine analysis using the flowave ocean energy research facility. *Renewable Energy*, *190*, 232-250.

Badshah, M., Badshah, S., & Jan, S. (2020). Comparison of computational fluid dynamics and fluid structure interaction models for the performance prediction of tidal current turbines. *Journal of Ocean Engineering and Science*, *5*(2), 164-172.

Badshah, M., Badshah, S., & Kadir, K. (2018). Fluid structure interaction modelling of tidal turbine performance and structural loads in a velocity shear environment. *Energies*, *11*(7).

Bahaj, A. S. (2013). Marine current energy conversion: the dawn of a new era in electricity production. *Philosophical Transactions of the Royal Society A: Mathematical, Physical and Engineering Sciences*, *371*(1985), 20120500.

Baratchi, F., Jeans, T., & Gerber, A. (2020). Assessment of blade element actuator disk method for simulations of ducted tidal turbines. *Renewable Energy*, *154*, 290-304.

Behrouzi, F., Nakisa, M., Maimun, A., & Ahmed, Y. M. (2016). Global renewable energy and its potential in malaysia: A review of hydrokinetic turbine technology. *Renewable and Sustainable Energy Reviews*, *62*, 1270-1281.

Belloni, C., Willden, R., & Houlsby, G. (2017). An investigation of ducted and open-centre tidal turbines employing cfd-embedded bem. *Renewable Energy*, *108*, 622-634.

Bermúdez, M., Cea, L., Puertas, J., Conde, A., Martín, A., & Baztán, J. (2017). Hydraulic model study of the intake-outlet of a pumped-storage hydropower plant. *Eng. Appl. Comput. Fluid Mech.*, *11*(1), 483-495.

Borg, M. G., Xiao, Q., Allsop, S., Incecik, A., & Peyrard, C. (2020). A numerical performance analysis of a ducted, high-solidity tidal turbine. *Renewable Energy*, *159*, 663-682.

Borg, M. G., Xiao, Q., Allsop, S., Incecik, A., & Peyrard, C. (2021). A numerical structural analysis of ducted, high-solidity, fibre-composite tidal turbine rotor configurations in real flow conditions. *Ocean Engineering*, *233*, 109087.

Cindori, M., Čajić, P., Džijan, I., Juretić, F., & Kozmar, H. (2022). A comparison of major steady rans approaches to engineering abl simulations. *Journal of Wind Engineering and Industrial Aerodynamics*, *221*, 104867.

DHV Turbines Ltd. (2022). *Company homepage.* Retrieved 2022-05-18, from `http://www.dhvturbines.com`

El-Sawy, M., Shehata, A. S., Elbatran, A. A., & Tawfiq, A. (2022). Numerical simulation of flow in hydrokinetic turbine channel to improve its efficiency by using first and second-law efficiency analysis. *Ocean Engineering*, *244*, 110400.

Feng, B., Liu, X., Ying, Y., Si, Y., Zhang, D., & Qian, P. (2022). Research on the tandem arrangement of the ducted horizontal-axis tidal turbine. *Energy Conversion and Management*, *258*, 115546.

Fleming, C. F., & Willden, R. H. (2016). Analysis of bi-directional ducted tidal turbine performance. *International Journal of Marine Energy*, *16*, 162-173.

Gabl, R., Achleitner, S., Neuner, J., & Aufleger, M. (2014). Accuracy analysis of a physical scale model using the example of an asymmetric orifice. *Flow Measurement and Instrumentation*, *36*, 36-46.

Gabl, R., Burchell, J., Hill, M., & Ingram, D. (2022). Geometry generation for dhv tidal turbine – basic python code and implementation in ansys-cfx and rhinoceros. *Edinburgh DataShare*. Retrieved 2022-05-18, from `https://doi.org/10.7488/ds/3455`

Gabl, R., & Righetti, M. (2018). Design criteria for a type of asymmetric orifice in a surge tank using cfd. *Eng. Appl. Comput. Fluid Mech.*, *12*(1), 397-410.

Gu, Y., Lin, Y., Xu, Q., Liu, H., & Li, W. (2018). Blade-pitch system for tidal current turbines with reduced variation pitch control strategy based on tidal current velocity preview. *Renewable Energy*, *115*, 149-158.

Hardisty, J. (2008). Modelling and testing the vertical axis, impulse rotor tidal power pontoon. *Journal of Marine Engineering & Technology*, *7*(1), 1-9.

He, J.-w., Zhao, W.-w., Wan, D.-c., & Wang, Y.-q. (2022). Numerical study of free end effect of cylinder with low aspect ratios on vortex induced motion. *Journal of Hydrodynamics*, *34*(1), 106–115.

Hua-Ming, W., Xiao-Kun, Q., Lin, C., Lu-Qiong, T., & Qiao-Rui, W. (2020). Numerical study on energy-converging efficiency of the ducts of vertical axis tidal current turbine in restricted water. *Ocean Engineering*, *210*, 107320.

Huang, B., Gong, Y., Wu, R., Wang, P., Chen, J., & Wu, P. (2022). Study on hydrodynamic performance of a horizontal axis tidal turbine with a lobed ejector. *Ocean Engineering*, *248*, 110769.

Ke, S., Wen-Quan, W., & Yan, Y. (2020). The hydrodynamic performance of a tidal-stream turbine in shear flow. *Ocean Engineering*, *199*, 107035.

Khamlaj, T. A., & Rumpfkeil, M. (2018b). Optimization study of shrouded horizontal axis wind turbine. In *2018 wind energy symposium.* Retrieved from `https://arc.aiaa.org/doi/abs/10.2514/6.2018-0996`

Khamlaj, T. A., & Rumpfkeil, M. P. (2018a). Analysis and optimization of ducted wind

turbines. *Energy*, *162*, 1234-1252.
Khan, M., Bhuyan, G., Iqbal, M., & Quaicoe, J. (2009). Hydrokinetic energy conversion systems and assessment of horizontal and vertical axis turbines for river and tidal applications: A technology status review. *Applied Energy*, *86*(10), 1823-1835.
Khojasteh, D., Lewis, M., Tavakoli, S., Farzadkhoo, M., Felder, S., Iglesias, G., & Glamore, W. (2022). Sea level rise will change estuarine tidal energy: A review. *Renewable and Sustainable Energy Reviews*, *156*, 111855.
Kirke, B. (2006). Developments in ducted water current turbines. *Tidal paper*, *25*, 04.
Kirke, B. (2011). Tests on ducted and bare helical and straight blade darrieus hydrokinetic turbines. *Renewable Energy*, *36*(11), 3013-3022.
Lee, S. O., Seong, H., & Kang, J. W. (2018). Flow-induced vibration of a radial gate at various opening heights. *Eng. Appl. Comput. Fluid Mech.*, *12*(1), 567-583.
Liu, H., Li, Y., Lin, Y., Li, W., & Gu, Y. (2020). Load reduction for two-bladed horizontal-axis tidal current turbines based on individual pitch control. *Ocean Engineering*, *207*, 107183.
Liu, W., Liu, L., Wu, H., Chen, Y., Zheng, X., Li, N., & Zhang, Z. (2022). Performance analysis and offshore applications of the diffuser augmented tidal turbines. *Ships and Offshore Structures*, *0*(0), 1-10.
Liu, Z., Wang, Z.-m., Shi, H.-d., & Qu, H.-l. (2019). Numerical study of a guide-vane-augmented vertical darrieus tidal-current-turbine. *J. of Hydrodynamics*, *31*(3), 522–530.
Maduka, M., & Li, C. (2021). Numerical study of ducted turbines in bi-directional tidal flows. *Eng. Appl. Comput. Fluid Mech.*, *15*(1), 194-209.
Menter, F. (1993). Zonal two equation k-w turbulence models for aerodynamic flows. In *23rd fluid dynamics, plasmadynamics, and lasers conference.*
Menter, F. (1994). Two-equation eddy-viscosity turbulence models for engineering applications. *AIAA Journal*, *32*(8), 1598-1605.
Menter, F. R., Kuntz, M., & Langtry, R. (2003). Ten years of industrial experience with the sst turbulence model. *Turbulence, heat and mass transfer*, *4*(1), 625–632.
Modali, P. K., Vinod, A., & Banerjee, A. (2021). Towards a better understanding of yawed turbine wake for efficient wake steering in tidal arrays. *Renewable Energy*, *177*, 482-494.
Mosbahi, M., Elgasri, S., Lajnef, M., Mosbahi, B., & Driss, Z. (2021). Performance enhancement of a twisted savonius hydrokinetic turbine with an upstream deflector. *International Journal of Green Energy*, *18*(1), 51-65.
Mulu, B. G., Cervantes, M. J., Devals, C., Vu, T. C., & Guibault, F. (2015). Simulation-based investigation of unsteady flow in near-hub region of a kaplan turbine with experimental comparison. *Eng. Appl. Comput. Fluid Mech.*, *9*(1), 139-156.
Nachtane, M., Tarfaoui, M., Goda, I., & Rouway, M. (2020). A review on the technologies, design considerations and numerical models of tidal current turbines. *Renewable Energy*, *157*, 1274-1288.
Noorollahi, Y., Ghanbari, S., & Tahani, M. (2020). Numerical analysis of a small ducted wind turbine for performance improvement. *Int. J. of Sustainable Energy*, *39*(3), 290-307.
Nunes, M. M., Brasil Junior, A. C., & Oliveira, T. F. (2020). Systematic review of diffuser-augmented horizontal-axis turbines. *Renewable and Sustainable Energy Rev.*, *133*, 110075.
Patel, V. K., & Patel, R. S. (2022). Optimization of an angle between the deflector plates and its orientation to enhance the energy efficiency of savonius hydrokinetic turbine for dual rotor configuration. *International Journal of Green Energy*, *19*(5), 476-489.
Picone, C., Sinagra, M., Aricó, C., & Tucciarelli, T. (2021). Numerical analysis of a new cross-flow type hydraulic turbine for high head and low flow rate. *Eng. Appl. Comput. Fluid Mech.*, *15*(1), 1491-1507.
Pisetta, G., Le Mestre, R., & Viola, I. M. (2022). Morphing blades for tidal turbines: A theoretical study. *Renewable Energy*, *183*, 802-819.
qi Wang, S., Xu, G., qing Zhu, R., & Wang, K. (2018). Hydrodynamic analysis of vertical-axis tidal current turbine with surging and yawing coupled motions. *Ocean Engineering*, *155*, 42-54.
Rehman, Z. U., Badshah, S., Rafique, A. F., Badshah, M., Jan, S., & Amjad, M. (2021).

Effect of a support tower on the performance and wake of a tidal current turbine. *Energies*, *14*(4).

Richter, W., Vereide, K., Mauko, G., Havrevoll, O. H., Schneider, J., & Zenz, G. (2021). Retrofitting of pressurized sand traps in hydropower plants. *Water*, *13*(18), 2515.

Roshanmanesh, S., Hayati, F., & Papaelias, M. (2020). Chapter 10 - tidal turbines. In M. Papaelias, F. P. G. Márquez, & A. Karyotakis (Eds.), *Non-destructive testing and condition monitoring techniques for renewable energy industrial assets* (p. 143-158). Boston: Butterworth-Heinemann.

Sarkar, D., & Savory, E. (2021, 02). Numerical Modeling of Freestream Turbulence Decay Using Different Commercial Computational Fluid Dynamics Codes. *Journal of Fluids Engineering*, *143*(4). (041503)

Sun, K., Ji, R., Zhang, J., Li, Y., & Wang, B. (2021). Investigations on the hydrodynamic interference of the multi-rotor vertical axis tidal current turbine. *Renewable Energy*, *169*, 752-764.

Sun, K., Ma, G., Wang, H., & Li, Z. (2019). Hydrodynamic performance of a vertical axis tidal current turbine with angular speed fluctuation. *Ships and Offshore Structures*, *14*(sup1), 311-319.

Sun, K., Yi, Y., Zhang, J., Zhang, J., Haider Zaidi, S. S., & Sun, S. (2022). Influence of blade numbers on start-up performance of vertical axis tidal current turbines. *Ocean Engineering*, *243*, 110314.

Ullah, H., Hussain, M., Abbas, N., Ahmad, H., Amer, M., & Noman, M. (2019). Numerical investigation of modal and fatigue performance of a horizontal axis tidal current turbine using fluid–structure interaction. *J. of Ocean Engineering and Science*, *4*(4), 328-337.

Walker, S., & Thies, P. (2021). A review of component and system reliability in tidal turbine deployments. *Renewable and Sustainable Energy Reviews*, *151*, 111495.

Ward-Smith, A. J. (1980). *Internal fluid flow-the fluid dynamics of flow in pipes and ducts* (Vol. 81). Clarendon Press, Oxford.

Yi, P., Wang, Y., Sun, X., Huang, D., & Zheng, Z. (2017). The effect of variations in first- and second-order derivatives on airfoil aerodynamic performance. *Eng. Appl. Comput. Fluid Mech.*, *11*(1), 54-68.